Natural Hazards
https://doi.org/10.1007/s11069-025-07335-8

ORIGINAL PAPER

A novel framework for flood susceptibility assessment using hybrid analytic hierarchy process-based machine learning methods

Chiranjit Singha[1] · Neha Chakraborty[2] · Satiprasad Sahoo[3,4] · Quoc Bao Pham[5] · Yunqing Xuan[6]

Received: 1 December 2024 / Accepted: 24 April 2025

Abstract
This study evaluates the effectiveness of the analytic hierarchy process (AHP) based on six machine learning models in predicting flood susceptibility in the Dwarakeswar river basin in Eastern India. Fifteen flood conditioning factors were employed as input predictors. The dataset underwent a series of pre-processing procedures, including conducting a statistical Pearson correlation, ordinary least squares (OLS), and multi-collinearity analysis, to identify the best flood-contributing factors. Additionally, the Information Gain Ratio (InGR) feature selection technique was utilized to assess the relevance of features. The accuracy of the models during the validation phases was assessed using various statistical metrics such as accuracy, kappa score, sensitivity, specificity, positive predictive value, negative predictive value, and the area under the receiver operating characteristic curve (AUC). Although all models demonstrated robust flood prediction abilities (AUC > 0.988), the AHP-Gradient Boosting Machine (GBM) model exhibited the highest performance (AUC = 0.996). This indicates that, among the models examined, the AHP-GBM model holds significant promise for evaluating flood-prone regions and facilitating effective planning and management of flood hazards. This model identified 12.68% and 5.14% of the study area as very high and high flood susceptibility zones, respectively. The SHapley Additive exPlanations (SHAP) analysis shows that the Modified Normalized Difference Water Index (MNDWI), rainfall, elevation, Normalized Difference Vegetation Index (NDVI), proximity to rivers, drainage density, and Terrain Ruggedness Indices (TRI) are the best influences on flood probability. Based on the climate projections from future Coupled Model Intercomparison Project Phase 6 (CMIP6) models (SSP2 4.5, SSP5 8.5), the southern region of the study area has been pinpointed as a hotspot for flooding vulnerability, with a susceptibility level classified as very high, encompassing 16.68% of the area.

Keywords Flood susceptibility mapping (FSM) · Analytic hierarchy process · Machine learning · Remote sensing

Extended author information available on the last page of the article

1 Introduction

Floods are recognized as the most catastrophic natural hazard globally, overshadowing various other hydro-meteorological risks (Wubalem et al. 2021). These hazards primarily stem from prolonged periods of intense rainfall, snowfall, landslides, climate and land use shifts, and sudden glacier lake outbursts. Moreover, the severity of floods is notably influenced by human activities such as faulty dam construction, rapid urbanization, deforestation, and population expansion (Tehrany et al. 2018). In contrast, flood hazard incorporates not only the likelihood of flooding but also the characteristics of flood events, including magnitude, frequency, duration, and depth. Floods, occurring worldwide, unleash devastating impacts on the environment, wreaking havoc on human infrastructure, transportation networks, and agricultural sectors and leading to loss of lives (Islam et al. 2021; Arabameri et al. 2022; Fatah and Mustafa 2022; Vilasan and Kapse 2022). Numerous regions, including the Ganges-Brahmaputra basin (India-Bangladesh), and the Mississippi Delta (US state), are particularly prone to flooding. Worldwide, floods stand out as the most devastating of all hydro-climatic natural occurrences, impacting millions each year. Between 1995 and 2015, approximately 150,061 flood events occurred, resulting in about 157,000 fatalities and rendering nearly 75 million people homeless each year (Islam et al. 2021). The top eight countries most affected by floods include India (2013), China (1887, 1931, 1935), Bangladesh (1974), Guatemala (1949), Iran (1954), Venezuela (1999), Peru (1941), Japan (1953), and many more (Swain et al. 2020), and others, as highlighted by the World Resources Institute. Notable historical floods have occurred in China, Bangladesh, Guatemala, Venezuela, and many other regions.

India, a prominent Southeast Asian country, witnesses approximately 320 million people affected by floods annually (Mitra et al. 2022). The nation's economy relies heavily on agriculture, leading to a significant population residing in flood-prone river valleys and coastal plains. Flood occurrences in India are primarily attributed to monsoon seasons, with 60% of the damage stemming from riverine floods and the remaining 40% from heavy rainfall and cyclones (Samanta et al. 2018a, b). Over the period from 1953 to 2009, India suffered 92,000 deaths and incurred an economic loss of $200 billion due to floods (Tripathi 2015). Notable instances include the submersion of three-quarters of Patna city in 1971 and 1975, flooding in Kolkata in 1978 and 2000, and inundation in Delhi in 1977 and 1978. In West Bengal, 111 blocks across 18 districts are at risk of flooding, constituting about 42% of the region (Samal et al. 2014). The Gangetic Delta, particularly prone to flooding, experiences significant property damage annually. The Bhagirathi-Hooghly River basin in West Bengal has faced devastating floods in various years, including 1956, 1959, 1978, 1995, 1998, and 1999 (National Disaster Management Authority, India, NDMA 2021). In the Dwarakeswar river basin, rainfall predominantly occurs during the monsoon season, from June to mid-October, with recorded flood events in 1984, 1987, 1993, 1995, 1999, 2000, 2007, 2009, 2011, 2013, 2014, 2016, and 2017 (Roy 2019). Anticipated socio-economic development, deforestation, and climate change are expected to exacerbate flood impacts in the future. Consequently, the identification of flood-prone areas becomes paramount in mitigating future disasters. Hirabayashi et al. (2021) examined future flood risk projections based on Coupled Model Intercomparison Project Phase 6 (CMIP6) climate models. The study underscores the correlation between global warming and the potential increase in flood exposure, particularly as populations grow, emphasizing the urgency of proactive decision-making.

Flood susceptibility refers to the likelihood of flooding based on inherent physical and environmental factors like topography, soil, land use, and proximity to water, typically representing a static assessment regardless of flood timing or intensity. Flood susceptibility mapping (FSM) is an essential tool for emergency planning and effective flood risk management, enabling the identification of high-risk areas and facilitating measures to minimize losses and damages caused by climate-induced flood disasters (Sun et al. 2021). FSM is more than just identifying hazards; it is about crafting tailored strategies for flood risk management. These maps, requiring less data than hazard and risk analyses, serve as crucial tools for preliminary assessments of potential flood events (Nguyen 2022). Given the impact of climate change and land use alterations, flood susceptibility analyses are vital for developing early warning systems and strategies to prevent or mitigate future floods (Tabari 2020). As climate shifts and land use patterns change, FSM gains significance in proactively pinpointing flood-prone areas and guiding preventive measures to bolster resilience against this natural threat (Shu et al. 2023). In the studies reviewed, researchers employed various variables contributing to flooding, presenting a complex challenge in FSM. There are no set guidelines for determining flood-influencing factors, with the selection depending on the study area's physical and environmental traits and data availability. The process of identifying and selecting suitable variables driving flooding is intricate, directly influencing the accuracy and reliability of the resultant FSM. Typically, FSM analysis approaches fall into three primary groupings: (1) hydrological approaches, (2) multi-criteria decision analysis (MCDA), and (3) machine learning (ML) models. While hydrological and hydrodynamic models allow for precise flood magnitude predictions, they are often resource-intensive and require comprehensive datasets (Zeng et al. 2024; Gai et al. 2019; Khosravi et al. 2019; Vashist and Singh 2023; Kannapiran and Bhaskar 2024). MCDA is straightforward to compute and understand, but it heavily depends on expert judgments and faces challenges associated with redundant data layers, leading to subjectivity, and heightened computational demands (Kaya, and Derin 2021; Swain et al. 2020; Edamo et al. 2022; Wang et al. 2019).

In recent times, FSM has undergone a noteworthy transition from traditional expert judgments to the adoption of diverse ML techniques, representing a significant advancement in the discipline. ML techniques such as Extreme Gradient Boosting (XGB) (Zhu et al. 2024), Random Forest (RF) (Hitouri et al. 2024), Gradient Boosting Machine (GBM) (Singha et al. 2022); Support Vector Machines (SVM) (Liu et al. 2022), Decision Tree (DT) (Seydi et al. 2023), Artificial Neural Networks (ANN) (Islam et al. 2023), Naïve Bayes (NB) (Singha and Swain 2022), classification and regression tree (CART) (Ahmadlou et al. 2022) and multivariate adaptive regression spline (MARS) (Mosavi et al. 2022) have been incorporated into FSM evaluation owing to their exceptional ability to manage heightened complexity.

The combination of MCDA, ML, Geographic Information System (GIS), and Remote Sensing (RS) has proven to be an effective tool for spatial analysis in hazard evaluation. Nachappa et al. (2020) evaluated the effectiveness of two MCDA models (i.e. analytic hierarchy process (AHP), analytic network process (ANP)) and two ML models (i.e. RF, SVM) for predicting flood susceptibility in Austria, finding that ML models, with an Area Under the Curve (AUC) greater than 0.87, performed slightly better than the MCDA models. The methods used to analyze FSM have evolved from traditional expert assessments to statistical methods utilizing large datasets and ML techniques. ML algorithms are steadily improving and have become increasingly popular for predicting FSM.

Statistical and analytical techniques typically depend on limited field data, which often fail to fully account for the complex and nonlinear interactions among flood-related factors.

Developing accurate and dependable FSM models is crucial, particularly when leveraging ML, to effectively support disaster risk management and promote sustainable growth in flood-prone areas. The lack of comprehensive FSM data hampers timely and efficient disaster response and limits the implementation of adaptive measures. Advancing research in this field is key to creating models reliably detecting flood-prone zones, offering crucial insights that help communities improve their readiness and ability to withstand flood-related hazards. Given the complexities and uncertainties involved in classifying features for FSM assessment, numerous studies have chosen to expand the variety of feature data (i.e., input data) to improve the accuracy and effectiveness of their models (Hosseini et al. 2020). Thus, conducting flood susceptibility assessment using MCDA-based ML with a satisfactory accuracy level by pinpointing critical features through data reduction on smaller samples is significantly important, even though the accuracy of this approach may slightly lag that of models using extensive data resources. These hybrid models have been proven to improve prediction precision, thus furthering the effectiveness of flood susceptibility mapping methods (Plataridis and Mallios 2023; Talukdar et al. 2022; Ghobadi et al. 2024).

Previous studies showed the slow processing MCDA approach including bivariate frequency ratio (FR), Knowledge-Driven (KD), Fuzzy Logic (FL), Logistic Regression and Dempster-Shafer-based evidential belief function (EBF) with minimal accuracy for FSM in Dwarakeswar river basin (Ghosh et al. 2023; Malik et al. 2020). Nsangou et al. (2022) demonstrated an FSM model using AHP in the Mfoundi watershed of Central Africa, incorporating both natural and human-induced factors. The outcomes of the model indicated an AUC of approximately 84%. Vilasan and Kapse (2022) generated flood susceptibility maps for Ernakulam district, India, utilizing remote sensing data and GIS, employing both the AHP and Fuzzy-AHP methods. The AUC values were 0.75 and 0.81 for the AHP and Fuzzy-AHP methods, respectively. Conventional MCDA techniques are capable of addressing various factors, but they often struggle with issues such as slow execution and the complexity of assigning accurate weights challenges that become more pronounced when used alongside complex ML algorithms. Moreover, a notable limitation in current studies is the difficulty in precisely mapping the spatial and temporal dynamics of flood occurrences and ensuring that flood data remains consistently updated. This study introduces a novel hybrid method for current and future FSM focused on the Dwarakeswar River basin in India, aiming to overcome existing research limitations. By leveraging multi-temporal Synthetic Aperture Radar (SAR) data and an Otsu thresholding technique, we develop a continuously updated flood inventory that captures the dynamic behavior of flood events. The methodology offers three significant innovations.

This study addresses the following research questions: (i) What factors are associated with FSM in river catchments? and (ii) Does a hybrid AHP-based ML approach achieve optimal accuracy in FSM probability? (iii) What are the scenarios of future flood probability distribution?

To address these research questions, the study is guided by three primary objectives:

(i) To generate a real-time flood inventory for use in FSM modeling, enhanced by integrating historical data from the Global Flood Database (GFD.v1, 2000–2018).
(ii) To develop an innovative hybrid FSM model by combining 15 flood-inducing parameters and training and validating it with a suite of novel ML algorithms (including RF, XGB, GBM, glmboost, glmnet, and rda) alongside the AHP method. This fusion aims to improve the reliability, interoperability, and consistency of flood susceptibility assessments.

(iii) This work enhances standard FSM by incorporating climate projections based on CMIP6 pathways (SSP2-4.5 and SSP5-8.5). This approach provides a forward-looking perspective on how climate change might affect flood risks, aiding adaptive planning and disaster preparedness efforts within the Dwarakeswar River basin.

Unlike previous research, this study utilizes a novel flood inventory generated from Sentinel-1 data and incorporates climatic projections from CMIP6 to enhance the accuracy of flood susceptibility predictions. A distinctive feature of this research is the use of Explainable Artificial Intelligence (XAI), specifically SHAP analysis, to understand the sensitivity of model parameters, bridging a gap in the literature and enhancing the transparency of the modeling process. This approach not only improves theoretical understanding but also supports decision-making for mitigating the impacts of flooding. Overall, the study offers new insights into FSM in Eastern India, contributes to disaster environmental management, and proposes strategies to reduce future flood risks, benefiting human society. The region has faced frequent flooding events and continues to be highly vulnerable to inundation, largely due to its unique landform features and prevailing weather patterns. Further, this study offers valuable insights into FSM assessment for flood-prone river catchment areas by establishing a robust and transparent modeling approach. A comprehensive methodology was employed to analyze FSM, encompassing several objectives: Initially, a detailed flood inventory dataset was constructed using freely available Sentinel-1 SAR satellite imagery to outline flood and non-flood areas, while also integrating factors of flood-contributing factors. The dataset underwent pre-processing steps, including a Pearson correlation, ordinary least squares (OLS), multi-collinearity test to identify and eliminate redundant contributing factors. In addition, the Information Gain Ratio (InGR) feature selection technique was used to determine feature importance. Advanced ML algorithms such as RF, XGB, GBM, glmboost, glmnet, and rda were fused with the AHP weightage of the factors utilized to generate the FSM model. Next, this method is implemented to generate future FSM using the CMIP6 datasets for both Shared Socioeconomic Pathway, i.e. SSP2 4.5 and SS5 8.5. These maps offer valuable insights into areas prone to flooding by considering identified factors that contribute to flooding. Following this, the model's performance underwent thorough evaluation using a range of statistical metrics, including kappa coefficient, accuracy, sensitivity, specificity, positive predictive value (PPV), negative predictive value (NPV), and AUC. Furthermore, the variation of SHAP analysis was utilized to interpret and elucidate the significance of flood-contributing factors within the predictive models, thereby enhancing the interpretability of the model and providing insights into the mechanisms underlying flood susceptibility.

2 Study area

The Dwarakeswar River, also known as Dhalkishore, is a significant river in the western part of West Bengal. Its drainage area spans from latitudes 23°32′00" N to 23° 40′25" N and longitudes 86°31′08″ E to 87°47′58" E (Fig. 1), covering a vast area of 4356.6 km^2 (Ghosh 2024). The Dwarakeswar River, originating from the Tilboni hill in Purulia district, flows through Bankura, Hooghly, and partially through Bardhaman and West Midnapore districts of West Bengal, India, before intersecting the Shilabati River near Ghatal to form the Rupnarayan River. The river basin serves as a transitional area between the Ganga Brahmaputra Delta and the Chhotanagpur Plateau, featuring varied landforms

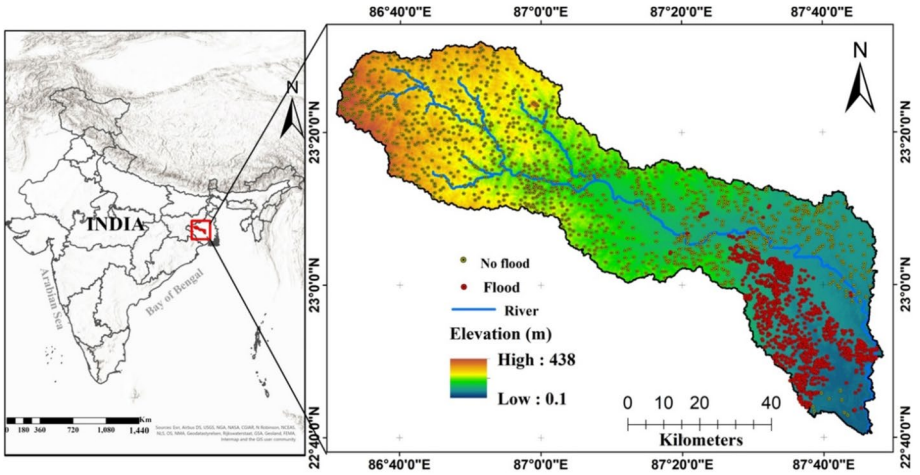

Fig. 1 Study area location map

from erosional hilly terrain to alluvial plains. This catchment area is subject to a monsoon climate characterized by considerable fluctuations in seasonal temperaturespeaking at an average of 32.55 °C during summer and dipping to 18.98 °C in winter with yearly rainfall ranging from 1400 to 1500 mm. The Dwarakeswar River experiences significant fluctuations in discharge, with September's average discharge around 130 tm^3 ts^{-1} and peaks exceeding 2000 m^3 s^{-1}, contrasting sharply with June's average of just 16.96 m^3 s^{-1}. This dramatic discharge level variation makes the river prone to instability and frequent, severe flood events. The basin's soil is primarily lateritic, especially in the western region of Bankura district. With a population of over 3 million, the basin faces challenges from agricultural pollution, with rice as the main crop, alongside efforts to diversify agriculture with oilseeds, pulses, and vegetables to enhance productivity.

3 Methodology

Figure 2 showed the methodological flowchart of this study aiming to provide an overview of the entire process, encompassing stages such as the creation of a flood inventory map, development of flood conditioning factors, assessment of these factors using information Pearson correlation, OLS, multi-collinearity, InGR and tests, and the application of various ML techniques (i.e. RF, XGB, GBM, glmboost, glmnet and rda) with AHP weightage factors for FSM modeling. The SHAP analysis provided detailed insights into the contributions of individual features to the model explanation. Ultimately, this research delved into forecasting future FSM using the CMIP6 datasets.

3.1 Flood inventory map generation

The integration of the GPS field survey and the Sentinel-1 Ground Range Detected GRD (S1) data were utilized to map flood inventory in this study area. The Google Earth Engine (GEE) platform was used to access the pre-processed S1 imagery from February 2020 to October 2023. All the flood inventory information was produced using 121 S1 C band

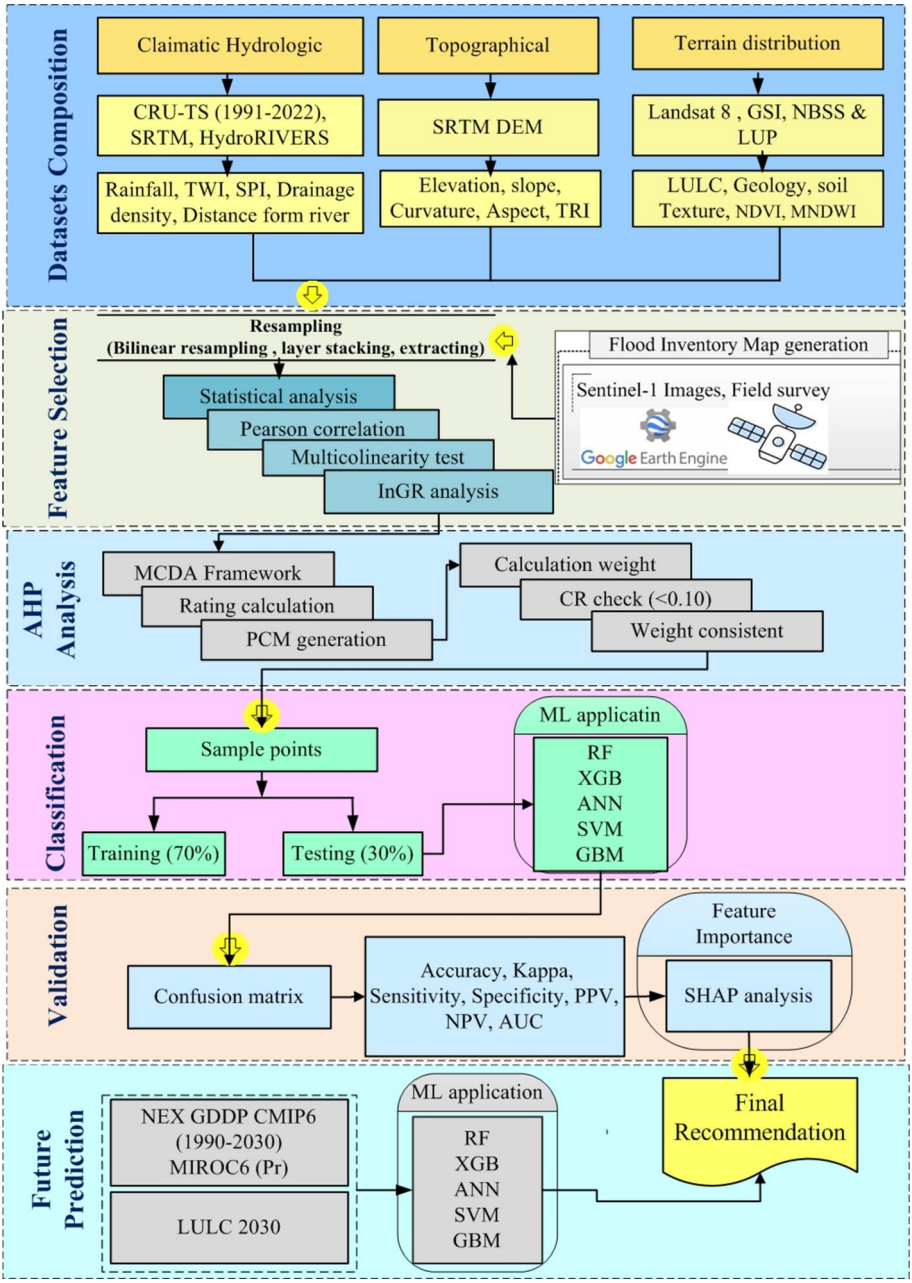

Fig. 2 Schematic illustration of the suggested analytical framework for flood susceptibility mapping

(VV/VH) tiles. Table 1 shows the S1 imagery acquisition dates employed in this study. S1 data sourced from GEE underwent pre-processing to eliminate noise via speckle filtering. Subsequently, the S1 imagery captured during flood occurrences between 2020 and 2023 was analyzed to map flood areas within the Dwarakesawr River Basin. The classification

Table 1 Multi temporal acquisition of descending Sentinel-1C images for historical flood inventory mapping

Satellite	Reference image	Post flood image
S1C GRD (2020)	2020/02/04–2020/02/21 (VH/VV-6)	2020/06/03–2020/06/27 (VH-7), 2020/07/02–2020/07/26 (VH-8), 2020/08/02–2020/08/31 (VH-9), 2020/09/07–2020/09/24 (VV-6), 2020/10/01–2020/10/30(VV-9)
S1C GRD (2021)	2021/02/05–2021/02/25 (VH/VV-6)	2021/06/01–2021/07/01 (VH-6), 2021/07/04–2021/07/28 (VH-7), 2021/08/02–2021/08/26 (VH-6), 2021/09/02–2021/09/26 (VH-7), 2021/10/01–2021/10/25 (VH-6),
S1C GRD (2022)	2022/02/05–2022/02/25 (VH/VV-6)	2022/06/01–2022/07/01 (VH-6), 2022/07/04–2022/07/28 (VH-7), 2022/08/04–2022/08/28 (VV-5), 2022/09/02–2022/09/26 (VH-6), 2021/10/03–2021/10/27 (VV-4),
S1C GRD (2023)	2023/02/05–2023/02/24 (VH/VV-3)	2023/06/05–2023/06/29 (VH-4), 2023/07/06–2023/07/30 (VH-4), 2023/08/11–2023/08/23 (VV-4), 2023/09/04–2023/09/28 (VH-5), 2023/10/03–2023/10/27 (VV-5),

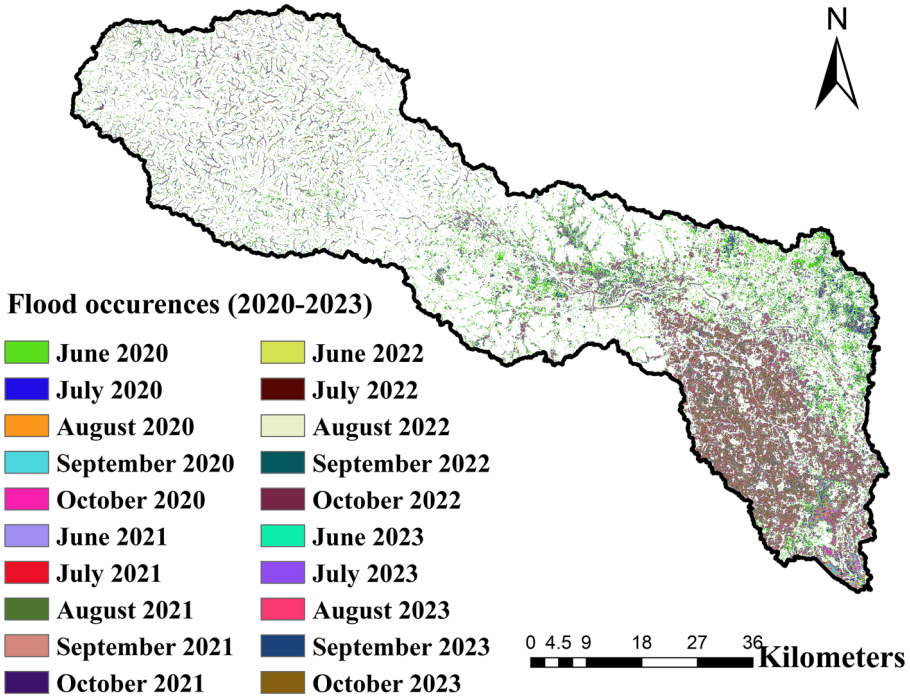

Fig. 3 S1C-based historical flood occurrences map generation (2020–2023)

of water and non-water pixels was conducted using Otsu's automatic thresholding method (Otsu 1979), which operates under the assumption of a bimodal histogram of pixel backscatter values through the differences of the pre and post-flood events. This technique employs a clustering approach to determine the threshold value, effectively segregating the classes into foreground (1 ~ flood) and background (0 ~ non-flood) categories. The optimal threshold value is derived by minimizing the weighted sum of intra-class variances, a process equivalent to maximizing the between-class variance, as outlined in Eq. (1). The flood inventory maps of the Dwarakeswar Basin produced through Otsu's thresholding algorithm underwent validation with the historical Global Flood database (2000–2018). The distinct flooded instances were condensed into 1,260 points for FSM utilization. Alongside the flooded samples, an equivalent number of non-flooded samples within the basin area were chosen arbitrarily. In machine learning models, values of 0 and 1 were respectively attributed to non-flooded and flooded points. Subsequently, the dataset was divided into a 70% training set and a 30% testing set for model training and evaluation purposes. All the historical time series of flood occurrence maps (2020–2023) are shown in Fig. 3. The detailed methodology for generating the flood inventory map is summarized in Fig. S1 (Fig. 4).

$$\sigma_B^2 = \omega_f \omega_{nf} \left(\mu_f - \mu_{nf} \right) \tag{1}$$

where σ_B^2 is the between-class variance, ω_f and ω_{nf} are mean values of flood pixel and non-flood pixel, and μ_f and μ_{nf} are the fraction of flood and non-flood pixels, respectively. An optimal threshold is identified, with pixel values falling below this threshold indicating areas affected by flooding.

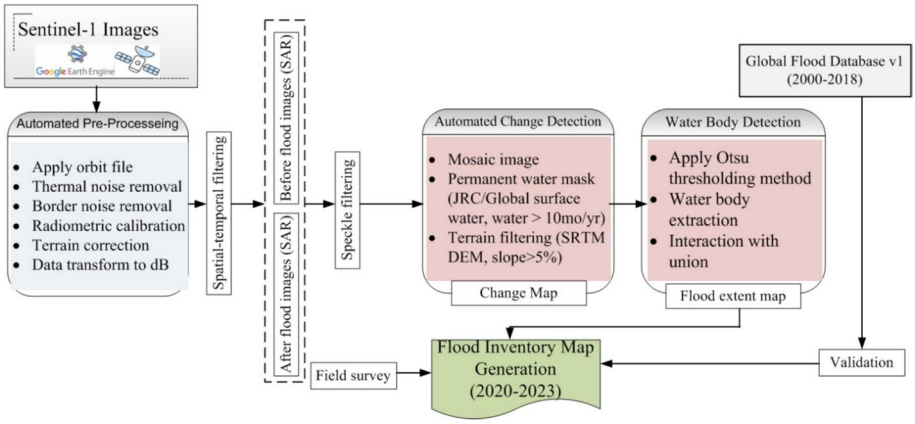

Fig. 4 Pre-processing steps of Sentinel 1C based on Otsu's method for flood inventory map generation

3.2 Selection of flood condition factors

Flood-influencing factors were selected based on previous studies to assist in the development of FSM models (Muthusamy et al. 2021; Al-Kindi and Alabri 2024; Das 2018; Ngo et al. 2018; Rahmati et al. 2019; Costache et al. 2020; Soltani et al. 2021). The suitability of these selected factors was subsequently assessed using techniques such as OLS, multicollinearity analysis, and the InGR algorithm. All the flood-influencing parameter sources and descriptive statistics are summarized in Table 2.

3.3 Flood condition factors

3.3.1 Topographical factor

The Shuttle Radar Topography Mission Digital Elevation Model (SRTM DEM), derived from C-band SAR, is widely used in FSM analysis due to its global coverage, free access, and moderate resolution (30 m) (Tehrany et al. 2014 and Rahmati et al. 2016). Topographical factors such as elevation, slope, aspect, curvature, and Terrain Ruggedness Index (TRI) were obtained from SRTM DEM, utilizing the GEE cloud platform. The study area exhibits a range of elevations from 0.1 m to 438 m (Fig. 5a). Flooding susceptibility decreases with increasing elevation, showing an inverse relationship (Mojaddadi et al. 2017; Muthusamy et al. 2021). Regions characterized by lower elevations, particularly those below 52 m, demonstrate notably higher susceptibility to floods, predominantly observed in the lower parts. Conversely, areas with higher elevations exceeding 177 m, mainly situated in the upper part of the study area, display lower susceptibility to flooding. Slope significantly impacts flood risk by controlling surface runoff (Skilodimou et al. 2021). The study area's slope varied significantly, with values ranging from below 1.39° to above 13.4° (Fig. 5b). Low-sloped areas, primarily located in the basin's middle and lower parts, demonstrated a high risk of flooding. In contrast, areas with steep slopes, over 13.4°, were sparsely distributed and showed a lower flood risk. Aspect influences how a slope segment interacts with elements such as wind, rainfall, sunlight, vegetation growth, evaporation, and soil moisture, affecting the balance between infiltration and runoff as well as the slope's orientation

Table 2 Flood-influencing parameters sources and descriptive statistics for FSM creation

Flood influencing factors	Data source	Description	Min	Max	Avg	Std	Type
Elevation	SRTM DEM (2014-09-23) (URL:https://earthexplorer.usgs.gov/)	Resolution 30 m	0.1	438	90.74	56.99	Numerical
Slope			0.1	44.33	1.91	1.32	Numerical
Curvature			−6.08	6.08	−0.024	0.22	Numerical
TWI			3.47	29.18	8.26	2.07	Numerical
TRI			0	71.81	2.76	1.87	Numerical
SPI			−11.51	13.12	−5.20	4.7	Numerical
Drainage density			0	2.75	0.742	0.53	Numerical
Aspect			–	–	–	–	Categorical
Distance from river	WWF/HydroSHEDS/v1/FreeFlowingRivers, Vector line, (URL:https://www.hydrosheds.org/)	Scale 1:50,000	0	7601	1247	1128	Numerical
Rainfall	CRU TS Data (Climate Research Unit Time Series Data) (1991–2022) (URL:https://crudata.uea.ac.uk/cru/data/hrg/)	Resolution 0.5°×0.5°	1280	1454	1347	49.64	Numerical
LULC	Landsat 8 2020 (URL:https://earthexplorer.usgs.gov/)	Resolution 30 m	–	–	–	–	Categorical
NDVI			−0.15	0.51	0.33	0.067	Numerical
MNDWI			−0.46	0.35	−0.092	0.056	Numerical
Soil	NBSS & LUP (National Bureau of Soil Science & Land Use Planning) (URL:https://nbsslup.icar.gov.in/)	Soil texture map	–	–	–	–	Categorical
Geology	GSI (Geological survey of India) (URL:www.gsi.gov.in)	Scale 1:50,000	–	–	–	–	Categorical

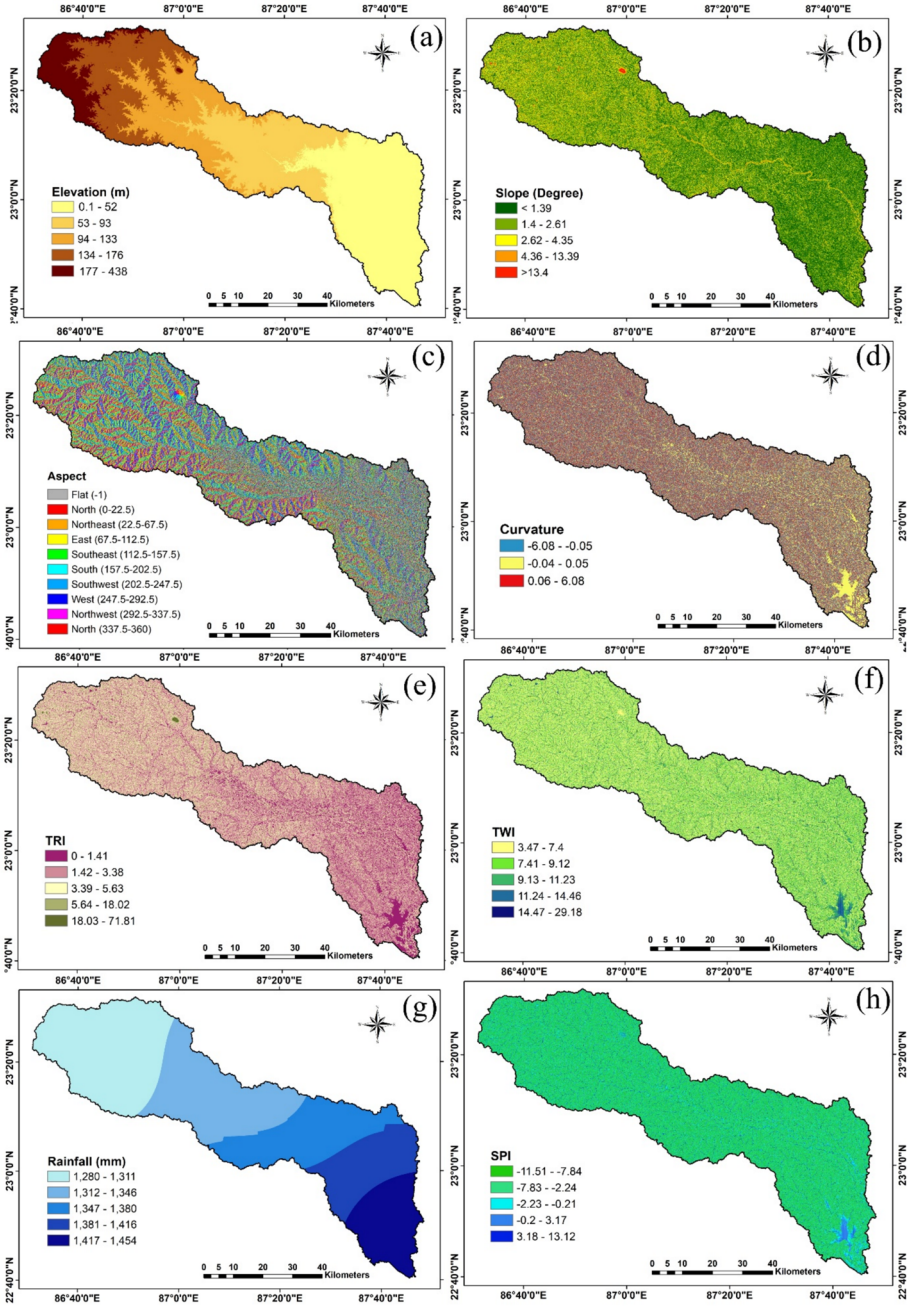

Fig. 5 The maps of the FCPs, including topographical factor **a**–**f**: **a** elevation, **b** slope, **c** aspect, **d** curvature, **e** TRI; climate hydrological factor **f**–**j**: **f** TWI, **g** rainfall, **h** SPI, **i** drainage density, **j** distance from river and terrain distribution factor **k**–**o**: **k** LULC, **l** geology, **m** soil texture, **n** NDVI, **o** MNDWI

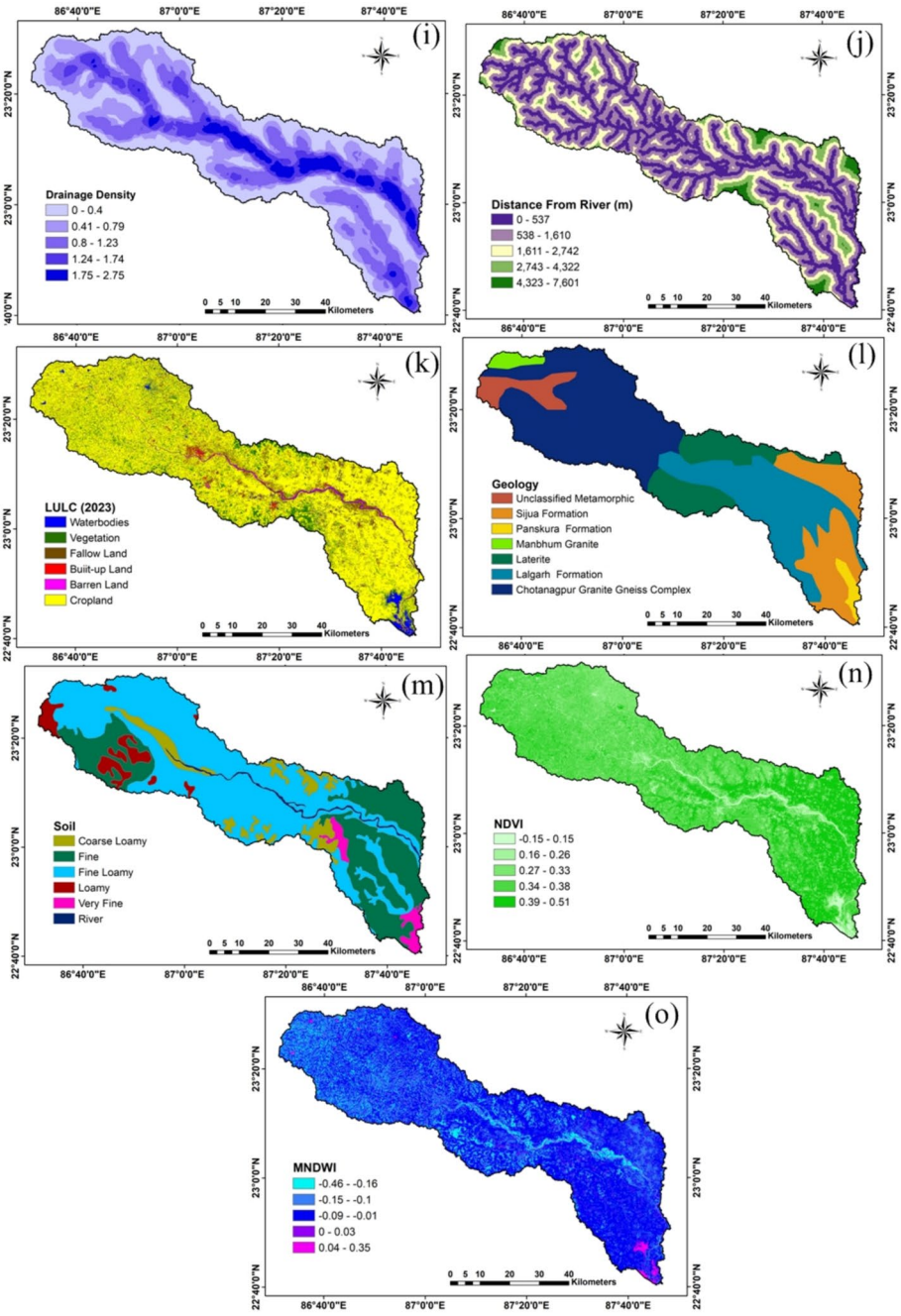

Fig. 5 (continued)

(Das and Pardeshi 2018). In this study, the aspect map was segmented into ten categories: (1) flat; (2) north (0–22.5 degrees); (3) northeast (22.5–67.5 degrees); (4) east (67.5–112.5 degrees); (5) southeast (112.5–157.5 degrees); (6) south (157.5–202.5 degrees); (7) southwest (202.5–247.5 degrees); (8) west (247.5–292.5 degrees); (9) northwest (292.5–337.5 degrees); and (10) north again (337.5–360 degrees) (Fig. 5c).

Curvature plays a pivotal role in governing surface water movement and infiltration processes (Al-Kindi and Alabri 2024). In this study, curvature values range from −6.08 to 6.08 (Fig. 5d). The curvature was categorized into concave (−6.08 to −0.05), flat (−0.05 to 0.05), and convex (0.05 to 6.08) subgroups. Positive curvature values denote areas with an upward convex gradient, indicating low susceptibility to flooding. Conversely, negative curvature values indicated areas with a concave gradient, suggesting high susceptibility to flooding. Areas with flat curvature, characterized by zero value, exhibited moderate vulnerability to flooding. TRI is a valuable metric for distinguishing between flat and uneven terrains (Pourali et al. 2014). Lower TRI values suggest areas more prone to flooding, such as floodplains adjacent to streams. In the study area, TRI values ranged from 0 to 71.81 (Fig. 5e), categorized into five distinct classes on the map. Regions with low TRI values (0 to 1.41) are highly susceptible to floods, whereas those with high TRI values (18.03 to 71.81) exhibit lower susceptibility.

3.3.2 Climatic and hydrological factors

This study examines several climatic and hydrological factors, including the Topographic Wetness Index (TWI), rainfall, Stream Power Index (SPI), drainage density, and the distance from the river. Among these, the TWI holds particular significance in assessing flood susceptibility, offering insights into how topography influences water flow, soil moisture, and accumulation within a river catchment area (Das 2018). The TWI map is derived from slope and flow accumulation data extracted from SRTM DEM data, with TWI calculated using Eq. 2 (Shahabi et al. 2020).

$$TWI = Ln\left(\frac{As}{tan\beta}\right) \tag{2}$$

where As represents the catchment area and β represents the slope (in degrees). Areas with higher TWI values are more susceptible to flooding than those with lower TWI values.

TWI values in the study area varied from 3.47 to 29.18 (Fig. 5f), with higher values (14.47 to 29.18) signalling an increased flood risk, and lower values (3.47 to 7.4) suggesting a reduced flood susceptibility.

In the study area, flooding is predominantly triggered by rainfall, with a direct correlation between precipitation levels and flood occurrence (Jenkins et al. 2018; Penki et al. 2023). Annual rainfall data from 1991 to 2022 were acquired from the Climate Research Unit-Time Series Data (CRU-TS Data) portal to produce the annual rainfall map. Employing the Inverse Distance Weighting (IDW) technique, the rainfall data were interpolated and subsequently classified using the Natural Breaks (Jenks) method within a GIS framework. The natural breaks method classifies data by identifying inherent patterns to maximize differences between classes and minimize variation within them for clearer, more coherent groupings (Jenks 1967). The resultant rainfall map delineates the study area into five distinct annual rainfall categories, ranging from 1280 to 1454 mm (Fig. 5g). As would be expected, regions characterized by higher rainfall values (1417–1454 mm) typically coincide with areas more susceptible to flooding, particularly observed in the lower basin

area. Conversely, regions with lower rainfall values (1280–1311 mm) correspond to areas less vulnerable to flooding, predominantly found in the upper basin region. Notably, the lower basin area exhibits a heightened susceptibility to flooding in comparison to the upper basin area.

Flood occurrences are notably affected by the SPI, which assesses both flow rate and erosion power in a particular area. A lower SPI value indicates a heightened flood risk (Ngo et al. 2018; Mitra et al. 2022). The SPI map is created using slope data and flow accumulation, typically derived from the SRTM DEM, with calculations based on Eq. (3) (Ali et al. 2020).

$$SPI = As \times tan\beta \tag{3}$$

Within the study area, the SPI values ranged from −11.51 to 13.12 (Fig. 5h), indicating varying levels of deposition or erosion potential across different locations. Negative SPI values suggest susceptibility to deposition, while positive values indicate erosive potential. Regions with lower SPI values are at higher risk of flooding, while those with higher SPI values are less prone to flooding.

The river networks were extracted from the HydroRIVERS dataset (accessed via URL: https://www.hydrosheds.org). Drainage density, reflecting the length of rivers per unit area, plays a vital role in flood management, with higher densities indicating elevated flood risks due to increased surface runoff (Mahmoud and Gan 2018; Rahmati et al. 2019). Utilizing the GIS line density tool, a drainage density map was generated, revealing values ranging from 0 to 2.75 km/km^2 across the region (Fig. 5i). This map was categorized into five classes, delineating areas with high drainage density (1.75–2.75 km/km^2) as highly susceptible to flooding, predominantly in the middle and lower riverside regions. Conversely, areas with low drainage density (0–0.4 km/km^2) are less prone to floods. Moreover, drainage density diminishes with distance from the river.

The distance from the river serves as a pivotal determinant in gauging a region's susceptibility to flooding, with a diminishing influence of the river as distance increases from its banks (Singha et al. 2024; Waqas et al. 2021). Euclidean distance tool was employed to generate the distance from the river map using the HydroRIVERS datasets. This map spans from 0 to 7601 m (Fig. 5j). Areas in close proximity to the river (0–537 m) exhibit heightened flood risk, while those situated farther away are less susceptible to flooding.

3.3.3 Terrain distribution factors

Land use and land cover (LULC) profoundly influence various hydrological processes, including infiltration rates, surface runoff accumulation, and surface-underground water interaction (Souissi et al. 2020; Costache et al. 2020). LULC data also encompass human activities such as settlements, industrial areas, and agriculture, reflecting both environmental impacts and natural cover distributions. Forested and vegetated regions typically exhibit high infiltration rates, whereas built-up and rocky areas experience lower rates, rendering them more prone to flooding (Hammami et al. 2019). The acquisition of LULC data involved obtaining a Landsat 8 image (2020) with minimal cloud cover (< 0.5%) from the United States Geological Survey (USGS) via the GEE server. LULC patterns were delineated using the random forest (RF) supervised classification technique within GEE. The classification identified six primary categories within the basin, including water bodies, vegetation cover, cropland, barren land, fallow land, and built-up areas (Fig. 5k). Water bodies and built-up areas are more prone to flooding,

while regions with dense vegetation are less susceptible. Geology plays a key role in influencing water runoff dynamics, which is integral to understanding flooding mechanisms (Kourgialas et al. 2011). The permeability and porosity of soil and rock formations directly impact processes like infiltration and runoff generation (Donnelly et al. 2006). The Geological Survey of India (GSI) provided the geology map used in this study (scale 1:50,000), delineating various formations such as the Panskura Formation, Sijua Formation, Lalgarh Formation, Laterite, Chotanagpur Granite Gneiss Complex, Manbhum Granite, and Unclassified Metamorphic (Fig. 5l). These formations exhibit diverse characteristics in terms of permeability and storage capacity, influencing their susceptibility to flooding events.

Soil texture significantly influences flood occurrence by regulating permeability pattern and surface runoff rate (Haghizadeh et al. 2017). Lower soil porosity results in slower infiltration rates, leading to increased surface runoff and flood risk. Clay soils, with their low porosity and limited infiltration, are more prone to flooding compared to loamy and sandy soils. The soil map utilized in this study, sourced from the National Bureau of Soil Survey and Land Use Planning (NBSS & LUP), delineates various soil types including river, very fine, fine, fine loamy, loamy, and coarse loamy (Fig. 5m). In the lower part of the study area, soil types exhibited high flood susceptibility due to their impermeability.

Furthermore, the existence of vegetation profoundly influences both infiltration capability and surface water movement, rendering Normalized Difference Vegetation Index (NDVI) a pivotal element in pinpointing flood-vulnerable areas (Soltani et al. 2021). Recognized for its efficacy, NDVI stands as one of the most extensively employed vegetation indices. Employing Landsat 8 imagery within GIS software facilitates the generation of an NDVI map, with NDVI values calculated using Eq. 4 (Rouse et al. 1974).

$$NDVI = (NIR - RED)/(NIR + RED) \tag{4}$$

where *NIR* represents the near-infrared band value and *RED* represents the red band value. The NDVI value is assessed across a spectrum from −1 to + 1, in which -1 denotes extensive water bodies and + 1 signifies dense vegetation cover. Therefore, areas exhibiting negative NDVI values are notably prone to flooding, whereas those showcasing positive NDVI values are linked to reduced susceptibility to flooding (Duong Thi et al. 2020). In this study,

the NDVI values observed within the study area varies between −0.15 and 0.51 (Fig. 5n). Lower NDVI values within the range of −0.15–0.15 indicated an elevated likelihood of flooding, whereas higher NDVI values, ranging from 0.39 to 0.51, implied a diminished susceptibility to flooding.

The Modified Normalized Difference Water Index (MNDWI) is highly effective in detecting water-related features compared to other indices, with higher values indicating increased flood susceptibility (Han-Qiu 2005). It is computed using Eq. 5 (Xu 2006).

$$MNDWI = (GREEN - SWIR1)/(GREEN + SWIR1) \tag{5}$$

where GREEN represents the green band and SWIR 1 the short-wave infrared band. MNDWI values typically range from −1 to + 1, where negative values signify an absence of water bodies and positive values indicate their presence. In this study, the MNDWI was classified into five categories from −0.46 to 0.35 (Fig. 5o). Higher MNDWI values (0.03 to 0.35) suggest greater flood susceptibility, while lower values (−0.46 to −0.16) imply reduced susceptibility.

3.4 OLS and multi-collinearity analysis

The OLS technique is a fundamental and extensively applied approach for linear regression analysis (Zdaniuk 2014). The reliability of OLS depends heavily on whether its core assumptions are met. It provides valuable insights into the relationships between variables, aiding in the decision-making approach.

Multicollinearity, a statistical test, enables the examination of the linear relationship among two or more explanatory variables. In this approach, the variance inflation factor (VIF) metric was utilized to identify and address unsuitable geo-environmental elements. Threshold values for VIF were established at < 10, respectively, to detect potential multicollinearity concerns (Singha et al. 2023). Strictly, multicollinearity is indicated when the TOL value is under 0.1 and the VIF exceeds 10, signifying strong correlation among predictors (Sahana et al. 2020). If these variables surpass these thresholds, it suggests the presence of multi-collinearity issues. Values between 1 and 5 imply moderate correlation, while a VIF of 5 + suggests significant multicollinearity, risking model reliability (Shrestha 2020).

3.5 Information gain ratio analysis

Prior to model training and validation, it is essential to evaluate the significance of flood-influencing parameters. This process entails assessing the statistical properties and correlation of each parameter with flooding. Implementing InGR metric analysis through scikit-learn in a Python-based Google Colab environment. Utilizing the InGR technique aids in pinpointing influential parameters for flood susceptibility analysis (Sameen et al. 2019). Each parameter receives an InGR value, serving as a metric for its importance, where higher values signify increased influence (Bui et al. 2020). The simplicity and efficacy of the InGR model render it well-suited for this study, computed through Eqs. (6–9) (Khodaei et al. 2025). The InGR enhances feature selection by addressing the bias of Information Gain (IG) toward features with many distinct values. Calculated as InGR, IG is divided by Split Information (SI), where IG measures entropy reduction from a data split, and SI represents the feature's intrinsic entropy InGR helps identify genuinely predictive attributes with reducing uncertainty. This normalization is particularly effective in DT algorithms, leading to more accurate and balanced models compared to using IG alone. Additionally, the entropy method was applied as a metric in DT algorithms to identify the optimal split during tree construction. It measures the level of impurity or disorder within a dataset, with values ranging from 0 (fully pure) to 1 (fully impure) (Quinlan 1986).

$$IG(X \cdot F) = \frac{Entropy(X) - Entropy(X \cdot F)}{Split\ Entropy(X \cdot F)} \tag{6}$$

$$Entropy(X) = -\sum_{i=1}^{2} \frac{\left(Y_i \cdot F\right)}{|X|} \log \frac{n\left(Y_i \cdot F\right)}{|X|} \tag{7}$$

$$Entropy(X \cdot F) = -\sum_{j=1}^{m} \frac{X_j}{|X|} Entropy(X) \tag{8}$$

$$Split\ Entropy(X \cdot F) = -\sum_{j=1}^{m} \frac{X_j}{|X|} \log_2 \frac{X_j}{|X|} \tag{9}$$

where X denotes the training dataset comprising n input samples, while $n(Y_i \cdot X)$ indicates the count of input samples that belong to the category Y_i (either flood or no flood).

3.6 AHP weightage estimation for flood condition factors

The AHP, proposed by Saaty (1980), is widely adopted for MCDA due to its efficacy in handling complex problems. It proves invaluable for resolving intricate problems and is frequently used for assigning weights or ratings to components (Supplementary Table S1). In this study, a comprehensive set of fifteen flood-influencing factors was integrated to establish the flood susceptible areas. Based on the experts' opinions, we developed a matrix table of each flood conditioning factor (Table 3). Flood hazard factors underwent evaluation on a scale from 1 to 9, with 1 indicating equal importance and 9 indicating one component's greater significance over another. Reciprocal values such as 1/1 and 1/9 were used to denote relative importance. These ratings, as per Penki et al. (2023), served to assess the weights assigned to the factors for conducting a multi-criteria evaluation of their impact on flood occurrence within the study area (Supplementary Table S2). The normalization of the matrix involved summing the values in each column and dividing each entry in the column by this sum, resulting in its normalized score (Supplementary Table S3). The total sum of each column is equal to 1. Criteria weights were then obtained using this normalized matrix, calculated by determining the arithmetic mean of each row in Supplementary Table S4. Subsequently, percentages for each thematic layer were computed based on the derived criteria weights. The Consistency Ratio (CR) serves as a measure to assess the pair-wise comparison of parameters and their sub-categories (Nguyen and Hoang 2023; Siddayao et al. 2014). It is determined using Eq. (10):

$$CR = CI/RCI \tag{10}$$

Here, CR represents the Consistency Ratio, CI denotes the Consistency Index, and RCI stands for the Random Consistency Index. The RCI values remain constant, as outlined by Saaty in Supplementary Table S2, for different n values and indexes. CI is calculated using Eq. (11):

$$CI = (\lambda \max - n)/(n-1) \tag{11}$$

where n signifies the number of factors, and λmax is the average value of the consistency vector. If the CR value is ≤ 0.1, the AHP result is considered acceptable. However, if the CR value exceeds > 0.1, it indicates that the obtained result does not align with the assessment objective and necessitates a revision of the method used (Saaty 1987).

3.7 Machine learning model application

To construct the FSM model, we utilized flood inventory as the dependent variable for prediction, employing binary values where 1 represents flood points and 0 represents non-flood points through the S1 SAR data. The numerous instances of flooding were condensed into 1,260 points for use in the FSM. Following this, the dataset was split into a 70% training set (882 samples) and a 30% testing set (378 samples). In this research, independent

Table 3 AHP rank and weights for the parameters of FSM in the Dwarakeswar river basin

Main Parameters	Rank	Normalized weight	Sub parameters	Area Cover (%)	Rank	Normalized weight	Susceptibility classes
Elevation	13	11.93	< 52	34.74	5	52.10	Very high
			52–93	21.13	4	21.91	High
			93–133	17.90	3	14.00	Moderate
			133–176	17.61	2	7.94	Low
			> 176	8.60	1	4.06	Very low
Slope	15	19.98	0–1.39	35.57	5	49.82	Very high
			1.39–2.61	38.99	4	27.59	High
			2.61–4.35	21.11	3	11.25	Moderate
			4.35–13.39	4.26	2	7.01	Low
			13.39–44.33	0.07	1	4.33	Very low
Rainfall	14	15.15	1280–1311	29.94	1	3.71	Very low
			1311–1346	24.31	2	6.02	Low
			1346–1380	18.63	3	12.82	Moderate
			1380–1461	14.04	4	27.84	High
			1461–1454	13.09	5	49.61	Very High
Drainage density	12	10.61	0–0.40	33.24	1	5.49	Very Low
			0.40–0.79	25.84	2	8.89	Low
			0.79–1.23	22.73	3	14.40	Moderate
			1.23–1.74	11.88	4	25.89	High
			1.74–2.75	6.30	5	45.33	Very high
Distance from river	10	7.52	0–536.56	29.55	5	40.02	Very high
			536.56–1609.67	19.67	4	25.82	High
			1609.67–2742.39	30.68	3	19.69	Moderate
			2742.39–4322.25	12.29	2	10.19	Low
			4322.25–7601.20	7.81	1	4.28	Very low

Table 3 (continued)

Main Parameters	Rank	Normalized weight	Sub parameters	Area Cover (%)	Rank	Normalized weight	Susceptibility classes
LULC	9	5.42	Waterbodies	4.18	6	41.63	Very high
			Builtup	1.01	5	24.66	High
			Barren land	0.52	4	15.46	Moderate
			Fallow land	7.57	3	8.82	Low
			Cropland	74.54	2	5.73	Low
			Vegetation	12.18	1	3.70	Very low
Soil texture	11	8.42	River	1.46	6	35.12	Very high
			Very fine	2.65	5	24.45	High
			Fine	28.91	4	16.13	Moderate
			Fine loamy	55.37	3	11.09	Moderate
			Loamy	4.55	2	8.06	Low
			Coarse loamy	7.06	1	5.15	Very low
Geology	8	4.92	Panskura formation	1.52	7	34.73	Very high
			Sijua formation	16.07	6	22.29	High
			Lalgarh formation	24.42	5	17.52	High
			Laterite	13.07	4	10.33	Moderate
			Chotanagpur granite gneiss Complex	38.17	3	7.60	Moderate
			Manbhum granite	1.72	2	4.76	Low
			Unclassified metamorphic	5.03	1	2.76	Very low
TWI	7	3.76	3.47–7.40	43.19	1	5.30	Very low
			7.40–9.12	31.68	2	8.51	Low
			9.12–11.23	16.10	3	12.03	Moderate
			11.23–14.46	7.15	4	24.28	High
			14.46–29.18	1.88	5	49.88	Very high

Table 3 (continued)

Main Parameters	Rank	Normalized weight	Sub parameters	Area Cover (%)	Rank	Normalized weight	Susceptibility classes
NDVI	6	3.12	−0.15–0.15	2.34	5	47.37	Very high
			0.15–0.26	6.82	4	28.55	High
			0.26–0.33	23.13	3	14.39	Moderate
			0.33–0.38	41.66	2	6.03	Low
			0.38–0.51	26.04	1	3.66	Very low
MNDWI	2	1.30	−0.46–−0.16	9.71	1	4.20	Very low
			−0.16–−0.1	28.45	2	6.22	Low
			−0.1–−0.01	58.54	3	12.22	Moderate
			0–0.03	0.86	4	25.95	High
			0.03–0.35	2.43	5	51.41	Very high
SPI	5	2.64	−11.51–−7.84	42.01	5	52.57	Very high
			−7.84–−2.24	25.07	4	25.35	High
			−2.24–−0.21	20.84	3	10.85	Moderate
			−0.21–3.17	9.99	2	6.95	Low
			3.17–13.12	2.09	1	4.28	Very low
TRI	1	1.17	0–1.41	14.34	5	39.89	Very high
			1.41–3.38	52.70	4	30.01	High
			3.38–5.63	26.84	3	17.11	Moderate
			5.63–18.02	6.04	2	9.31	Low
			18.02–71.81	0.08	1	3.68	Very low
Curvature	4	2.27	−6.08–−0.05 (Concave)	38.29	1	49.05	High
			−0.04–0.05 (Flat)	27.90	2	31.19	Moderate
			0.06 − 6.08 (Convex)	33.81	3	19.76	Low

Table 3 (continued)

Main Parameters	Rank	Normalized weight	Sub parameters	Area Cover (%)	Rank	Normalized weight	Susceptibility classes
Aspect	3	1.78	Flat	1.41	1	2.21	Very low
			North	7.63	4	4.36	Low
			North East	12.76	9	18.74	Very high
			East	13.23	6	7.72	Moderate
			South East	13.30	10	33.53	Very high
			South	12.36	8	11.68	High
			South West	11.89	7	8.46	High
			West	11.59	3	4.27	Low
			North West	11.73	2	4.22	Very low
			North	4.10	5	4.82	Moderate

parameters including elevation, slope, LULC, distance from the river, drainage density, rainfall, soil texture, geology, MNDWI, NDVI, TWI, aspect, SPI, TRI, and topographic curvature were employed. Consequently, hybrid AHP-based ensemble ML algorithms (specifically AHP-RF, AHP-XGB, AHP-GBM, AHP-glmboost, AHP-glmnet, and AHP-rda) were developed for both current and future FSM modeling. Hyperparameters of all ML were adjusted using tenfold cross-validation to stabilize the predictive capacity of the model. ML models are performed with the caret package in R software v3.4.4. Table 4 and Supplementary Fig. S1 summarize all the model tune parameters for FSM analysis.

3.7.1 Random forest (RF)

Developed by Breiman in 2001, RF is a powerful supervised ensemble machine learning technique for classification and regression. It improves the accuracy of individual classifiers through bagging and feature selection, generating multiple regression trees from randomly sampled data. This process culminates in a majority vote for classification, minimizing bias and overfitting. RF's methodology ensures broad applicability and robust performance by diversifying both the data and features used in training. In this study, the RF model was executed with 500 trees, a maximum tree depth of 10, and attempting 2 variables at each split.

3.7.2 Extreme gradient boosting (XGB)

XGB, a prominent tree-based algorithm in machine learning, stands out for its efficiency and accuracy. It excels due to its scalability, ability to handle different types of data, resilience to nonlinear relationships, natural feature selection process, and transparency.

XGB generates a predictive model as an ensemble of weak decision trees, employing gradient descent to minimize the loss function (Cui et al. 2017). This algorithm significantly decreases processing time and is versatile, being applicable to both regression and classification tasks. Key hyper-parameters were tune as follows: max_depth as 5, eta as 0.4, colsample_bytree as 0.6, gamma as 0.01, subsample as 1, min_child_weight as 0.05, and the objective function was set to binary: logistic.

Table 4 Best tune parameters of ML models for FSM analysis

Model	Tune parameter
RF	mtry = 5, verbose = FALSE, summaryFunction = 2, Type of random forest = classification, Number of trees = 500, variables split = 2
XGB	eta = 0.4, max_depth = 5, gamma = 0.01, colsample_bytree = 0.6, min_child_weight = 0.05, subsample = 1, objective = binary:logistic, validate_parameters = TRUE, niter = 100
GBM	Loss function = bernoulli, iterations = 150
Glmboost	Generalized Linear Models Fitted via Gradient Boosting, weights = NULL, offset = NULL,family = Gaussian(), boosting iterations: mstop = 150, Step size: 0.1,Offset: 0, coefficients = binomial, model = glm(family = 'binomial')
Glmnet	Family = binomial, alpha = 1, lambda = 0.00009, logistic function = modified Newton
rda	Gamma = 0.001, lambda = 0.5

3.7.3 Gradient boosting machine (GBM)

GBM was employed in supervised machine learning tasks, addressing various classification and regression challenges. GBM constructs a predictive ensemble from simple models, often decision trees (Strickland 2016). It focuses on three core elements: optimizing a specific loss function, employing weak learners for initial predictions, and using an additive approach to refine predictions by minimizing the loss function. Key tuning parameters for GBM involve Bernoulli loss function used with 150 iterations were performed. There were 15 predictors of which 15 had non-zero influence for FSM.

3.7.4 glmboost

The glmboost machine learning model is a powerful tool designed to address regression and classification tasks using generalized linear models (GLMs). It falls under the category of boosting algorithms, which enhance prediction accuracy by combining multiple weaker models (Mayr et al. 2014). glmboost applies the principles of gradient boosting to GLMs, enabling it to handle diverse data types such as binary, count, and continuous outcomes. It constructs an ensemble of GLMs incrementally, correcting errors made by previous models. Key features include flexibility in applying various statistical distribution models, robustness in handling noisy data, regularization to prevent overfitting, interpretability akin to standard GLMs, and tuning parameters like the number of boosting iterations: mstop is 150, step size is 0.1, offset parameters is 0.1, and family is Gaussian type for optimal performance in this study.

3.7.5 glmnet

Glmnet combines generalized linear models (GLMs) with regularization techniques to improve prediction accuracy and handle high-dimensional data efficiently with Lasso and Elastic Net Regularization parameters (Friedman et al. 2010). The optimal tuning parameters for the glmnet model in this study were determined as follows: the family parameter was set to binomial, alpha was specified as 1, lambda was adjusted to 0.00009, and the type of logistic function used was modified by Newton.

3.7.6 Regularized discriminant analysis (RDA)

RDA stands as a regularization method that merges elements of Linear Discriminant Analysis (LDA) and Quadratic Discriminant Analysis (QDA). It operates under the foundational framework established by LDA and QDA, and RDA introduces a novel approach to covariance estimation (Friedman 1989). This method involves blending the class-specific covariance matrices found in QDA with the overall covariance matrix used in LDA through the application of a tuning parameter λ. In this study, RDA was characterized by two parameters, gamma (0.001) and lambda (0.5).

3.7.7 Hybrid approach

The novel hybrid approach in this study combined the AHP method with all ML models for FSM analysis. It was determined that employing a hybrid approach was more

advantageous than using a single AI algorithm for FSM analysis (Singha et al. 2022). The integration of the AHP with ML enhances FSM modeling by combining expert-driven prioritization with data-driven prediction (Singha et al. 2025; Sahoo et al. 2024). AHP first assigns weights to flood-causative factors through pairwise comparisons, reclassifying input layers to reflect their relative influence. These weighted inputs are then fed into ML algorithms, which refine predictions using historical flood data. This hybrid approach improves accuracy in data-scarce regions by balancing expert knowledge with empirical pattern recognition while maintaining interpretability through transparent AHP weightings and robust ML validation.

3.8 Future flood susceptibility modeling

The study examined the future climatic analysis of FSM (1990–2030) using data from the CMIP6 MIROC6 datasets. This analysis was conducted under two distinct shared SSPs (i.e., SSP2 4.5 and SSP5 8.5) through the GEE platform. Future FSM for the study area was developed using datasets from CMIP6, incorporating key flood-related conditioning factors such as projected precipitation, 2030 LULC, along with topographic and environmental variables including elevation, slope, aspect, curvature, TRI, TWI, SPI, drainage density, proximity to rivers, geology, soil texture, NDVI, and MNDWI. Future FSM was conducted using R software version 4.3.2. LULC prediction was carried out on the GEE platform using a RF ML technique, specifically the.*smileRandomForest* classifier. LULC datasets from 2018 to 2022, sourced from the ESRI 10-m resolution collection, were used to train the model. A range of environmental predictor variables, including elevation, slope, NDVI, and MNDWI were also incorporated. The input parameters were prioritized using the AHP technique under the MCDA framework and utilized in six machine learning models to accurately forecast future FSM.

Training data was generated using the.*stratifiedSample* method to ensure balanced representation across all LULC classes. The dataset was divided into 80% for training (48,177 samples) and 20% for testing (11,919 samples) purposes. Model performance was evaluated using a confusion matrix to determine overall accuracy and kappa coefficient. Once validated, the trained model was used to forecast LULC for the years 2026 and 2030 at 4-year intervals, offering key insights into land use dynamics to support informed planning and resource management. These future conditioning factors were integrated with AHP weights and applied across six ML models to analyze future FSM in the study area. This analysis employed a tenfold repeated resampling technique for robustness. In this method, the dataset is split into 10 folds; the model trains on 9 and tests on 1, cycling through all folds. This process is repeated multiple times with different random splits to ensure reliable evaluation. It reduces bias and variance by training and testing the model across multiple randomized splits. It ensures more stable and reliable performance metrics, improving confidence in the model's generalizability for the FSM analysis (Shahabi et al. 2020; Singha et al. 2024).

3.9 Validation analysis

All the model's performance was assessed using practical and effective experimental techniques. In this research, key metrics such as accuracy, kappa score, sensitivity, specificity, NPV, PPV, and AUC were employed as primary measures for evaluating performance (Eqs. 12–18).

$$\text{Accuracy} = \frac{\text{TP} + \text{TN}}{\text{TP} + \text{TN} + \text{FP} + \text{FN}} \tag{12}$$

$$\text{Kappa coefficient} = \frac{P_{\text{obs}} - P_{\text{exp}}}{1 - P_{\text{exp}}} \tag{13}$$

$$\text{Sensitivity} = \frac{\text{TP}}{\text{TP} + \text{FN}} \tag{14}$$

$$\text{Specificity} = \frac{\text{TN}}{\text{TN} + \text{FP}} \tag{15}$$

$$PPV = \frac{\text{TP}}{\text{TP} + \text{FP}} \tag{16}$$

$$NPV = \frac{\text{TN}}{\text{TN} + \text{FN}} \tag{17}$$

$$\text{AUC} = \frac{\left(\sum \text{TP} + \sum \text{TN}\right)}{(\text{P} + \text{N})} \tag{18}$$

3.9.1 SHAP analysis

SHAP serves as a tool for interpreting the role of individual features in the predictions made by ML models. After training the ML model, SHAP values were computed to assess the impact of each feature on individual predictions. In this study, the best GBM model was executed for SHAP analysis. SHAP was calculated through Python's *shap* library on the Google Colab platform. It adopts an additive explanation framework, viewing each feature as a 'contributor' to the prediction, an idea derived from the principles of cooperative game theory (Lundberg and Lee 2017). For every predicted instance, the SHAP model produces a 'Shapley value' by aggregating the contributions of individual features, providing an explanation as follows in equation (Eq. 19):

$$g(z') = \emptyset_0 + \sum_{j=1}^{M} \emptyset_j z_j' \tag{19}$$

where the represents every factor, the explanation model, z′∈{0, 1}M represents the Top of Form coalition factor, M, the maximum union size, and ∅j∈R represents the factor acknowledgment for a variable j (Shapley value). In this study, the SHAP analysis is explained through different analyses, namely, SHAP score, waterfall plot, decision plot, SHAP heat map, force plot, etc. In this study, SHAP values are expressed relative to the model's baseline or expected value, similar to how the effects of a linear model are relative to its intercept. Values are centered around the model's average, reflecting shifts above or below the baseline. The SHAP sign indicates whether a feature increases or decreases the prediction, showing its directional and consistent impact. SHAP values indicate a feature contributes to the model's output: i.e., positive values increase the prediction (e.g., higher

flood susceptibility). Negative values decrease the prediction (e.g., lower flood susceptibility). The magnitude reflects the strength of the feature's influence.

4 Results

4.1 Multicollinearity and OLS analysis

Multicollinearity and OLS were evaluated across all 15 features (Table 5). Each feature's VIF did not surpass 10, indicating no serious multicollinearity among the features. Consequently, these features were considered appropriate inputs for the model. Elevation (6.04) and aspect (1.01) features exhibited the highest and lowest VIF values, respectively. According to the OLS analysis, curvature, TWI, SPI, drainage density, distance from river, rainfall, MNDWI, and NDVI were statistically significant at the 99% confidence level ($p < 0.001$) for the FSM. Furthermore, there is a 95% ($p < 0.01$) concordance observed in the elevation, aspect, and LULC features.

The results of Pearson's correlation analysis between flooding and its influencing factors are depicted in Fig. 6a. As per previous studies (Douglas et al. 2000), a higher correlation signifies an increased likelihood of flood occurrence. Key potential factors contributing to flood occurrence include rainfall, elevation, MNDWI, geology, NDVI, TRI, slope, TWI, and soil texture.

In the study area, most floods were observed in locations characterized by the Sijua and Lalagarh geological formations, fine soil type, elevation below 52 m, land cover consisting predominantly of cropland and bare land, low TRI values, high MNDWI values, rainfall

Table 5 Results for the OLS and multicollinearity test for FSM analysis

Feature	VIF	β	std err	t	P>|t|
Elevation	6.043	−0.0252	0.01	−2.528	0.012*
Slope	2.352	0.0097	0.01	0.966	0.334
Curvature	1.168	−0.0326	0.006	−5.139	0.00***
TWI	5.069	−0.044	0.011	−4.078	0.00***
TRI	1.966	0.0066	0.009	0.731	0.465
SPI	4.437	−0.0571	0.009	−6.565	0.00***
Drainage density	1.391	−0.0332	0.006	−5.715	0.00***
Aspect	1.011	−0.0088	0.004	−2.413	0.016*
Distance from river	1.307	0.0281	0.006	4.526	0.00***
Rainfall	5.807	0.207	0.009	23.582	0.00***
LULC	1.066	0.0363	0.012	3.073	0.01*
NDVI	1.669	−0.1244	0.008	−16.011	0.00***
MNDWI	1.635	0.1326	0.007	18.949	0.00***
Soil texture	1.086	−0.0018	0.009	−0.197	0.843
Geology	3.24	−0.0028	0.013	−0.221	0.825
	$R^2 = 0.879$	F-statistic = 1049	Durbin wat-son = 1.398	Prob > $chi^2 = 0.002$	

β ~ Coefficient; t ~ t test std err ~ Standard error, Robust standard errors ~ *$p < 0.05$, **$p < 0.01$, and, ***$p < 0.001$, F ~ Statistical, R^2 ~ Linear regression

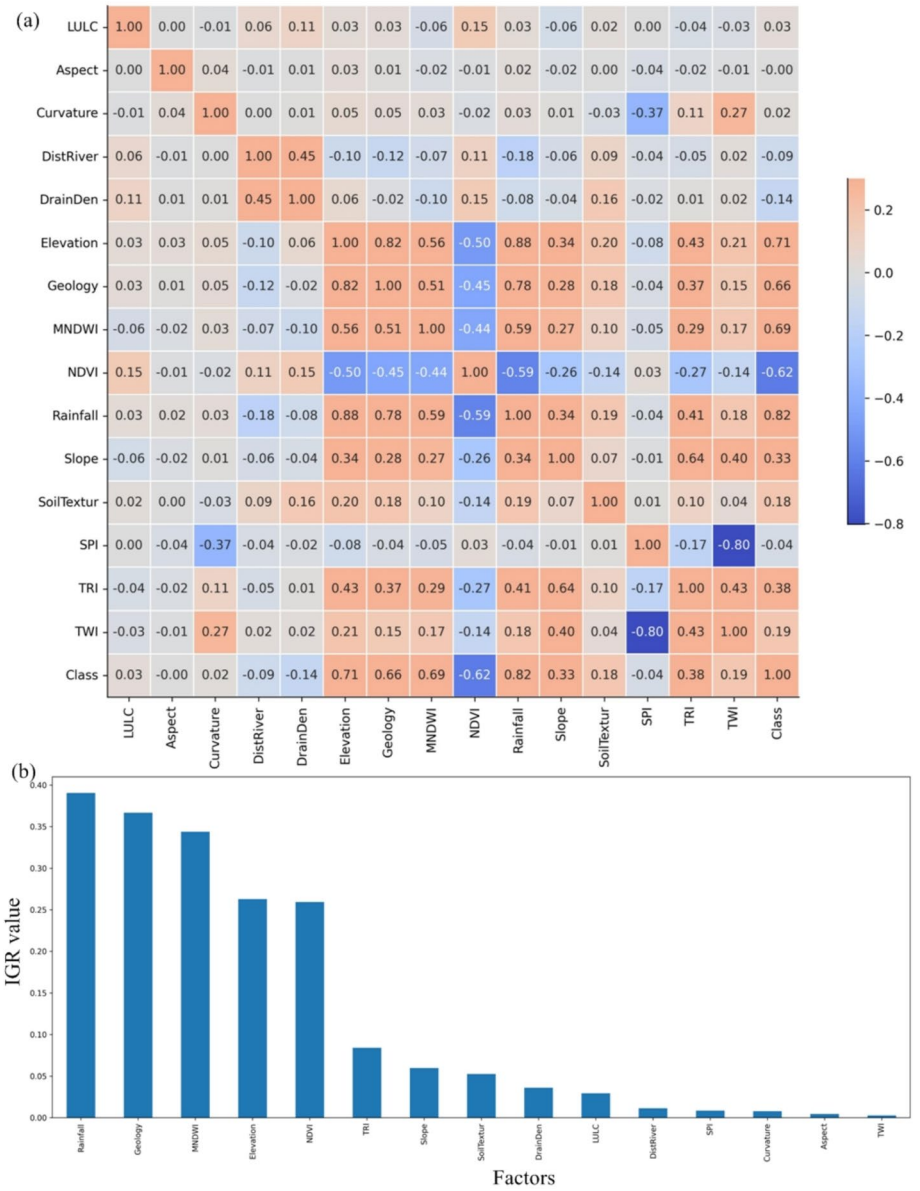

Fig. 6 **a** Correlation plot and **b** the feature importance of FCPs calculated by the Information Gain method

ranging from 1417 to 1454 mm, slope less than 1.3 degrees, TWI values ranging from −1.54 to 7.72, low NDVI values, and flat aspect.

4.2 Information gain ratio analysis

The results are depicted in Fig. 6b, illustrating the calculated InGR values for each parameter. According to the analysis, rainfall (0.390), geology (0.367), MNDWI (0.344), elevation (0.263), and NDVI (0.259) emerge as the most significant factors, showing high InGR values compared to other influencing factors. TRI (0.084), slope (0.060), soil texture (0.053), drainage density (0.036), and LULC (0.029) revealed medium significance. Conversely, distance to river (0.011), SPI (0.008), curvature (0.008), aspect (0.004), and TWI (0.003) exhibit minimal relevance in predicting FSM.

4.3 Flood susceptibility models

We utilized an AHP Pairwise Comparison Matrix (PCM) model to develop normalized weights for each criterion (Supplementary Table S5). According to the AHP results, slope received the highest weight (0.199), followed by rainfall, elevation, drainage density, soil texture, distance from river, LULC, geology, TWI, NDVI, SPI, curvature, aspect, MNDWI, and TRI. Hybrid AHP ML methods, namely AHP-RF, AHP-XGB, AHP-GBM, AHP-glmboost, AHP-glmnet, and AHP-rda, were employed to predict FSM using ArcGIS v.10.7.1 software. The six ML models were employed to compute FSM

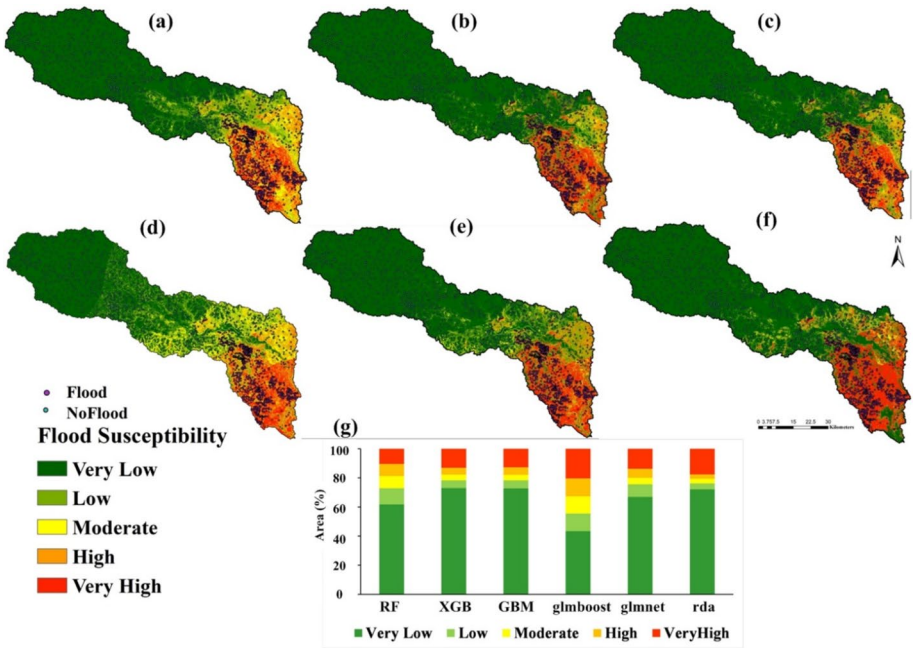

Fig. 7 Flood susceptibility maps **a**–**f**: **a** AHP-RF, **b** AHP-XGB, **c** AHP-GBM, **d** AHP-glmboost, **e** AHP-glmnet, and **f** AHP-rda and **g** area cover percentage

for each pixel in the basin (Fig. 7a–f). The susceptibility classes were classified into five classes (i.e., very low, low, moderate, high, and very high) with the natural breaks method in ArcGIS.

The results showed that, in the case of AHP-RF model, 61.82% area comes under the very low class, followed by low (11.11%), very high (10.43%), moderate (8.37%) and high (8.28%) classes (Fig. 7g). The percentages of area are 13.09%, 4.61%, 3.96%, 5.30%, and 73.05% for the very high, high, moderate, low, and very low classes, respectively, in the case of the AHP-XGB model. Findings revealed that AHP-GBM predicted 12.68% area as a very high class, followed by 5.14% area (high), 3.81% area (moderate), 5.55% area (low), and 72.82% area (very low), respectively. In the case of AHP-glmboost, AHP-glmnet, and AHP-rda models, the area percentages for very high classes are 20.37%, 13.71%, and 17.59%, respectively. In the case of very low flood susceptibility, the classes are 43.40%, 66.95%, and 72.10%, respectively. Across all maps, regions characterized by flat terrain and significant rainfall, particularly in the lower portions of the basin, are identified as having very high to high flood susceptibility zones.

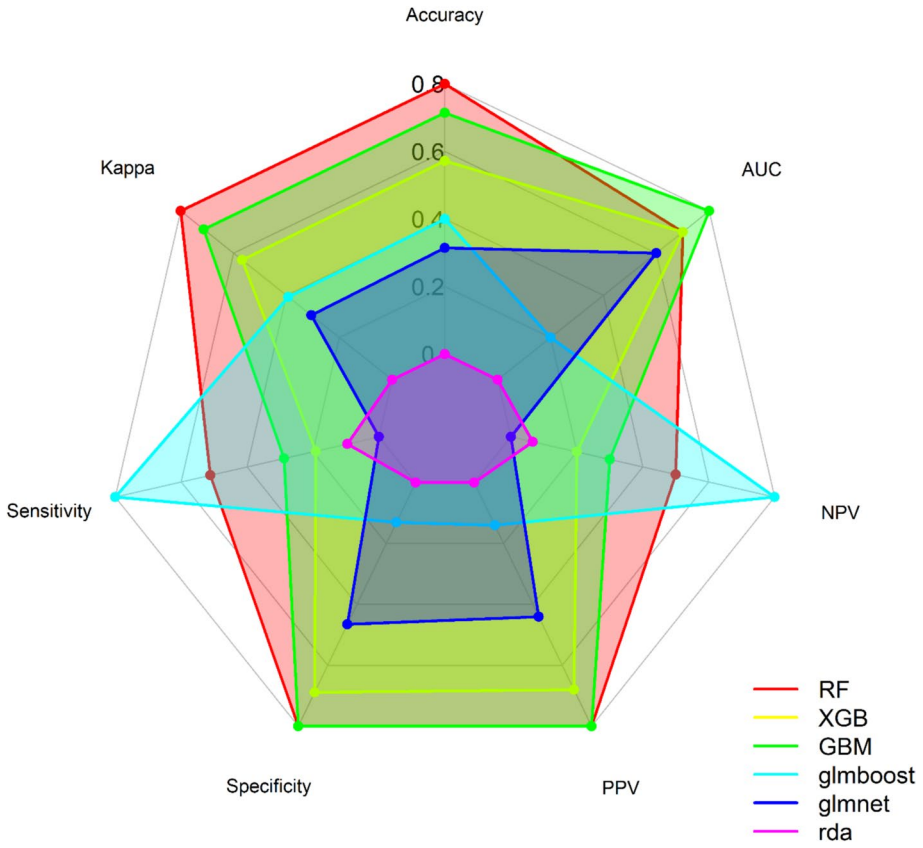

Fig. 8 Model performance of six ML algorithms for FSM modeling

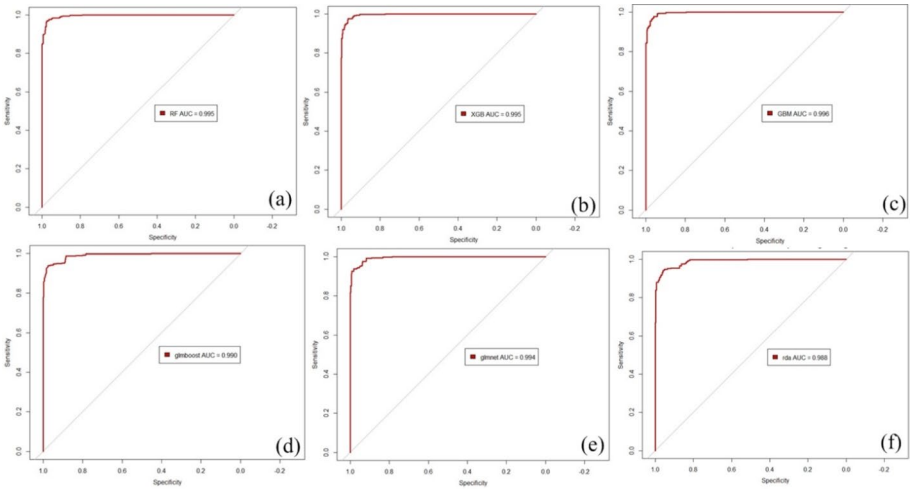

Fig. 9 AUC comparison among the different ML methods **a** RF, **b** XGB, **c** GBM, **d** glmboost, **e** glmnet, **f** rda

4.4 Validation analysis

Based on Fig. 8, the accuracy outcome of the RF model using the testing dataset is 0.968, which outperforms AHP-XGB (0.960), AHP-GBM (0.965), AHP-glmboost (0.954), AHP-glmnet (0.951), and AHP-rda (0.940). Figures 9a–f showed a comparison of the AUC scores across all ML methods used for generating FSM. The findings indicate that while all six FSMs demonstrated high predictive accuracy (AUC > 0.940), the AHP-GBM model emerged as the most effective for modeling FSM in this specific study area, achieving the highest AUC score of 0.996 (Fig. 9c). Illustration from the experimental findings of the kappa score, which varied between 0.881 and 0.936, was leveraged to improve model effectiveness. The results revealed that the glmboost model exhibited the greatest sensitivity, while the RF model demonstrated superior specificity compared to the other models. Subsequently, AHP-GBM and AHP-glmboosst showed the most favourable performance with a PPV and NPV Score of > 0.96.

4.5 Future flood susceptibility mapping analysis

Future climate CMIP6 MIROC6 data (SSP2 4.5 and SSP5 8.5 scenarios) were employed to delineate FSM zones within the study region, as illustrated in Fig. 10a–l. Future FSM was generated using CMIP6 datasets, incorporating projected precipitation, 2030 LULC, and key factors like topography, hydrology, geology, vegetation, and soil characteristics. For the 2030 LULC prediction, model validation showed 99.8% overall accuracy and a kappa coefficient of 0.997. These future conditioning factors, combined with AHP weights, were applied to six different ML models to assess future FSM in the area. A tenfold repeated resampling method was used in this analysis to ensure the robustness of the results.

The AHP-GBM, as the more precise model with SSP2 4.5 and SSP5 8.5 scenarios, revealed that the average susceptibility classes of very low, low, moderate, high, and very high resembled 64.63%, 6.51%, 4.26%, 8.94%, and 15.67% of the study area. In the SSP2 4.5 scenario, the average area of the entire study area to very low, low, moderate, high,

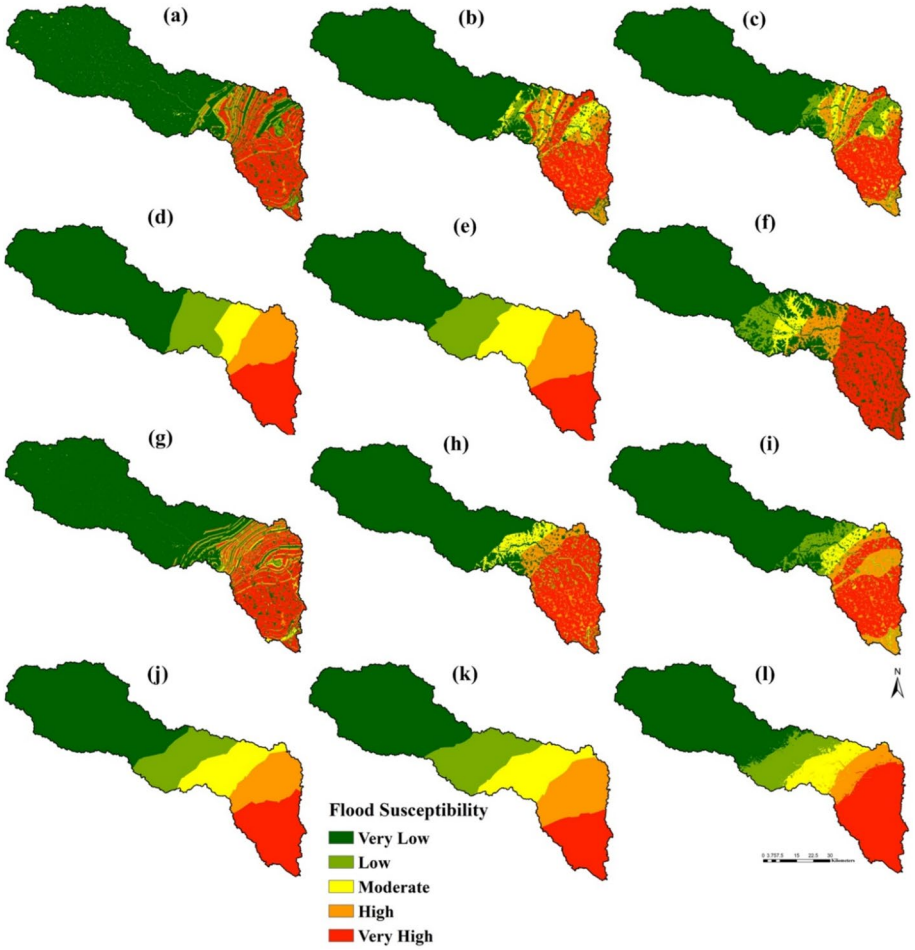

Fig. 10 Future flood susceptibility map of CMIP6 MIROC6 model: SSP2 4.5 scenario **a** RF, **b** XGB, **c** GBM, **d** glmboost, **e** glmnet, **f** rda and SSP5 8.5 scenario **g** RF, **h** XGB, **i** GBM, **j** glmboost, **k** glmnet, **l** rda

and very high flood susceptibility classes were 59.73%, 7.59%, 5.72%, 9.27%, and 17.69%, respectively (Supplementary Table S6). Similarly, with the SSP5 8.5 scenario, the average areas categorized as very low, low, moderate, high, and very high flood susceptibility classes accounted for 56.10%, 9.08%, 7.90%, 8.82%, and 18.10%, respectively. According to all models, regions situated in the southern part of the study area are identified as being more highly vulnerable hotspots to flooding, as forecasted by future climate patterns.

4.6 SHAP analysis

In this study, we introduced an interpretable method to control how the chosen model achieved an accurate outcome, along with its importance. According to the summary plot, we finalized that MNDWI, rainfall, elevation, NDVI, and drainage density were the most contributory factor for FSM analysis with the all-model prediction, whereas soil texture,

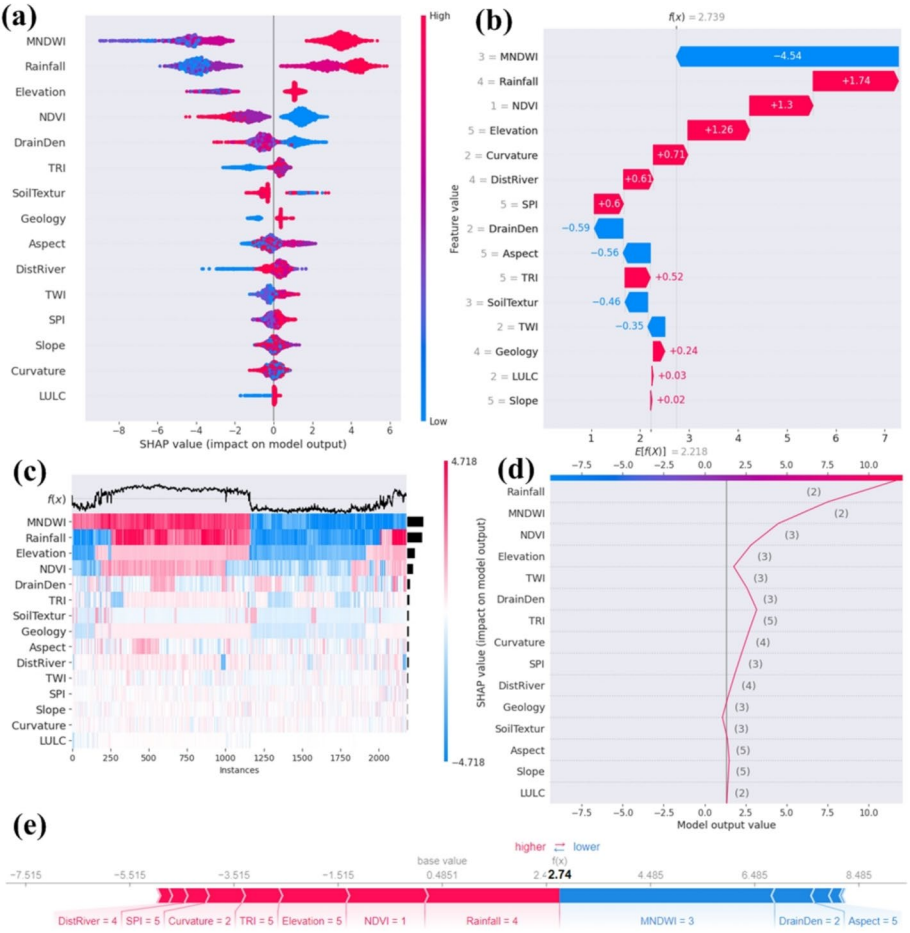

Fig. 11 SHAP plot **a** summary plot: SHAP feature impact values influence flood susceptibility predictions and their correlations. Red indicates higher susceptibility values, while blue signifies lower ones. This provides a concise view of the distribution and variation of SHAP values for each feature. Summary plots are organized by the importance of each feature to the model output, based on the sum of the absolute SHAP values for each feature. **b** Waterfall plot: these are intended to provide explanations for individual predictions, therefore, they require a single row from an Explanation object as input. A waterfall plot begins at the model's expected output value at the bottom, and each subsequent row demonstrates how each feature's positive (red) or negative (blue) contribution shifts the value from the expected output across the background dataset to the actual model output for that specific prediction., **c** Heatmap: the model's output is displayed above the heatmap matrix, centered on the explanation's base value, while the global significance of each model input is illustrated as a bar plot on the right side of the plot, using the *shap.order.abs.mean* measure as the default metric for overall importance **d** Decision plot: the horizontal axis depicts the model's output, measured in log odds. The plot is centered on the x-axis at the explainer's expected value. All SHAP values are relative to this expected value, similar to how linear model effects are relative to the intercept. The vertical axis lists the model's features. Each prediction is represented by a colored line, with the line intersecting the x-axis at the predicted value for that observation. This value determines the color of the line along a spectrum. As you move from the bottom to the top of the plot, SHAP values for each feature are added to the model's base value, illustrating each feature's contribution to the overall prediction. At the bottom of the plot, the observations converge at the expected value of the explainer. **e** Force plot: the horizontal layout of the force plot makes it difficult to display all significant features clearly. It reveals the key features that influence a model's output

geology, aspect, distance from river, and TWI were the moderate importance and SPI, slope, curvature, and LULC are least important (Fig. 11a). The water plot showed the global influencing flood condition factors like rainfall, NDVI, elevation, curvature, distance from river, and SPI had the positive impact where the MNDWI drainage density, aspect soil texture, and TWI had the negative impact of the flood susceptibility modelling (Fig. 11b). Using the heatmap plot function with a matrix of SHAP values generates a visualization where the instances are represented on the x-axis, the model inputs on the y-axis, and the SHAP values depicted using a color scale. This explanation revealed the overall importance of model accuracy achieved through the MNDWI, rainfall, elevation, and NDVI factors (Fig. 11c). In addition, Fig. 11d showed the variables improved accuracy for each pixel ordering, including rainfall, MNDWI, NDVI, elevation, TWI, drainage density, and the decision-making chances for flood susceptibility evaluation. The force plot effectively illustrates the decision-making process of the successive model. For the output shown in Fig. 11e, variables improving classification accuracy for each pixel included rainfall, NDVI, elevation, TRI, curvature, SPI, and distance from river; those decreasing classification accuracy included MNDWI, drainage density and aspect.

5 Discussion

Modeling and simulation platforms are vital tools that aid decision-makers by improving insights into flood hazard management. The varying designs and features of these models result in different levels of predictive accuracy and outcomes. Importantly, having a range of modeling options available equips policymakers with the resources to develop and implement robust environmental policies (Edamo et al. 2022). On the other hand, various approaches have been applied independently across different geographical areas for the mitigation of flood susceptibility. In the Dwaraeswar River basin, specifically in the lower part, data on flood susceptibility showed a wide distribution of areas at high risk. Both natural and human-made factors play a role in increasing the susceptibility of these regions to flooding. The winding course and meandering channels of rivers, particularly in streams with low gradients, increase the region's susceptibility to flooding. When the river reaches high water levels during peak times, it can overflow and lead to severe floods in Bihar and West Bengal. Land use plays a pivotal role in defining areas highly susceptible to floods. Malik et al. (2020) underscore the land-use changes triggered by river dynamics in the lower Dwarakeswar plains, where increased settlement and agricultural activities have influenced erosion and sediment deposition. Similarly, in the Dwarakeshwar river Basin, changes in LULC due to river dynamics have been documented by Sahoo et al. (2018). The relationship between river dynamics and land use is crucial, as it directly impacts the lives of those residing in floodplains. Variations in land use patterns, shaped by river dynamics, are key in evaluating the socioeconomic effects of river-related hazards. Notably, the expansion of residential areas and agriculture, alongside a reduction in grassland, highlights the consequences of agricultural expansion influenced in different districts by erosion, sediment deposition, and river path changes. The study found significant erosion and deposition in the middle of the river. The outcomes demonstrate that erosion and deposition show less impact on the upper and lower portions of the river. The topography of the Dwarakeswar basin includes both hilly and plain land areas. The study site has a maximum elevation in the extreme northeastern and eastern corners and a minimum elevation in the western and southwestern areas. The current research areas include fifteen blocks in

Bankura, five in Purulia, three in Burdwan, four in Hooghly, and three in the West Midnapore district. Bankura district covers the majority of the river basin.

For instance, Seydi et al. (2023) utilized RF to create a flood susceptibility map in Golestan province, Zhu et al. (2024) employed the XGB model in the Yangtze River Delta, and Stefanidis and Stathis (2013) implemented AHP in Greece's Kassandra Peninsula. Consequently, there is a need for comparative studies to assess the effectiveness of these models under identical conditions and to impartially evaluate their performance (Nachappa et al. 2020). This study analyzed and compared the predictive capabilities of six distinct modeling methods for mapping flood susceptibility in Dwarakeswar river basin, eastern India. These included hybrid AHP-based ML models and MCDA models, namely AHP-RF, AHP-XGB, AHP-GBM, AHP-gumboots, AHP-glmnet, and AHP-rda. According to the AUC score, the AHP-GBM (0.996) model demonstrated the highest predictive accuracy compared to the other models. A previous study showed that the AUC values ranged from 72 to 89% in this study area using the traditional MCDA approach (Ghosh et al. 2023; Malik et al. 2020). Furthermore, the advantage of ML models over MCDA ones stems from the uncertainty associated with the weighting of criteria based on expert knowledge in MCDA models. Nonetheless, all hybrid methods used in this study exhibited good to excellent accuracy. This study demonstrates the combination of AHP and ML methods, utilizing outcomes through a hybrid approach, which is distinctive and achieves improved accuracy in flood susceptibility mapping. A related study by Mfondoum et al. (2023) demonstrated the use of the Multi-Geoenvironmental Hazards Susceptibility (MGHS) tool, which integrates the AHP with ML across the North-Moungo region. We assessed the effectiveness of integrating MCDA-based AHP with ML techniques by analyzing and comparing the AUC values of both the standalone AHP and its hybrid models,

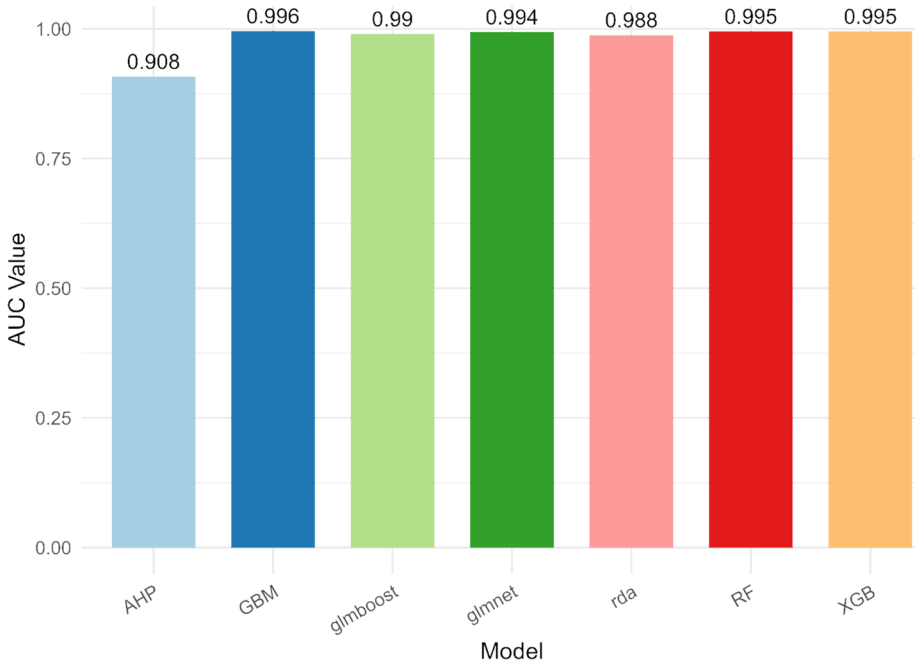

Fig. 12 Comparison of FSM assessment results using standalone AHP and hybrid AHP-ML models

Fig. 13 Flood susceptibility evaluation by **a** flood hazard zonation with Bhuvan, ISRO, India database **b** ▶ LULC changes with river discharge rate in Dwarakeswar river basin and **c** cropland risk map due to flood susceptibility level within the study area

as illustrated in Fig. 12. Figure 12 shows that standalone AHP had the lowest predictive accuracy (AUC = 0.908), while AHP-ML models performed better, with GBM achieving the highest AUC (0.996) and rda has the lowest (0.988). This confirms the superiority of AHP ML methods over AHP for FSM analysis. Moreover, the hybrid AHP-ML models consistently outperformed both individual approaches, demonstrating enhanced predictive performance through integration.

Several researchers have explored ensemble approaches for FSM. Tehrany et al. (2013) utilized an ensemble of multivariate and bivariate statistical models, finding that the ensemble model surpassed individual models. Similarly, Tehrany et al. (2014) developed new ensemble models using weights-of-evidence and SVM models, demonstrating their superiority over single models. Termeh et al. 2018 discussed novel ensembles of adaptive neuro-fuzzy inference system and nature-inspired algorithms, which exhibited improved prediction performance for flood susceptibility. This study reinforces these findings, showing that the hybrid model combining AHP with six ML models yielded superior flood susceptibility predictions.

The congruence in spatial delineation of high and very high flood susceptibility areas identified by RF-ANN, Fuzzy-RF, and ANN-Fuzzy models suggests that regions featuring extremely low elevation (< 10 m), substantial flow accumulation, concave topography, minimal slope, elevated wetness index, and close proximity to rivers are susceptible to flooding (Islam et al. 2023). With the optimal AHP-GBM model, our research revealed that 12.68% of the area was within the category of very high flood susceptibility, while 5.14% of the area was classified as high flood susceptibility. Low elevation, flat areas, minimal slope, high TWI primarily located in the basin's middle and lower parts, demonstrated a high risk of flood susceptibility. The AHP-GBM model outperformed other hybrids in FSM. In the Dwarakeswar River Basin, especially from northwest to southeast, high-risk zones were widespread due to both natural and human factors, as shown in Fig. 7c. Our results were validated using flood layers from the flood hazard atlas maps (2000–2020) available on Bhuvan, ISRO, India (Fig. 13a). These results were compared with flood hazard zones along the lower part of the Dwarakewar river, including the right and left banks in areas such as Daulat Chak, Gobindapur, Gangprasad, Dalapatipur, Syamsundarpur, Nanadangar, Ratanapur, and Gazipur were classified as high to very high flood susceptible regions. The moderate to high susceptible zone includes Hara, Ranghubati, Chutra, Nandpur, Srimanatapur, Shnsutra, Tentuietz, and Kenijun. Similarly, the upper part of the region, including Lodhasuti, Chhota, Narahipur, Patpur, Nischintapur, Tentulia, and Baijala, also shows low to moderate susceptibility to flood hazards within the study area.

Examining the influential factors through the InGR analysis unveiled that rainfall, elevation, slope, LULC, distance to road, TRI, and SPI exert a significant influence on FSM (Hosseini et al. 2020; Islam et al. 2021). These findings align with our study, which identified the most significant flood conditioning factors as rainfall (0.390), geology (0.367), MNDWI (0.344), elevation (0.263), and NDVI.

The examination of LULC in conjunction with FSM indicated that approximately 5.14% -12.68% of agricultural land lies within the high to very high risk zones, rendering them prone to frequent crop damage (Fig. 13c). A comparable study revealed (Singha and Swain 2022) that intense rainfall and the severe Cyclone Amphan (May 2020) led to flood

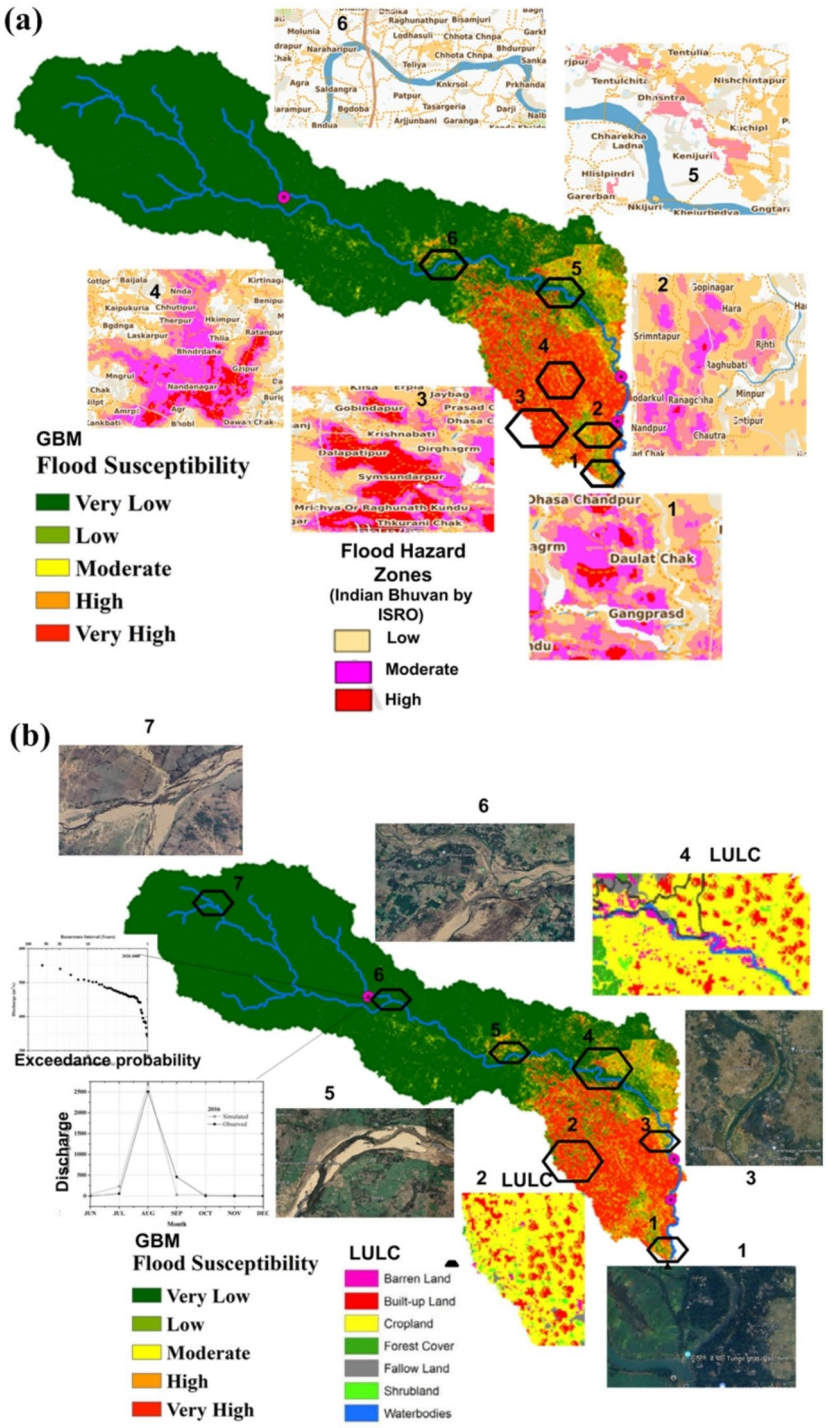
(a)
GBM
Flood Susceptibility
Very Low
Low
Moderate
High
Very High
Flood Hazard Zones
(Indian Bhuvan by ISRO)
Low
Moderate
High
(b)
Exceedance probability
Discharge
GBM
Flood Susceptibility
Very Low
Low
Moderate
High
Very High
LULC
Barren Land
Built-up Land
Cropland
Forest Cover
Fallow Land
Shrubland
Waterbodies
4 LULC
2 LULC

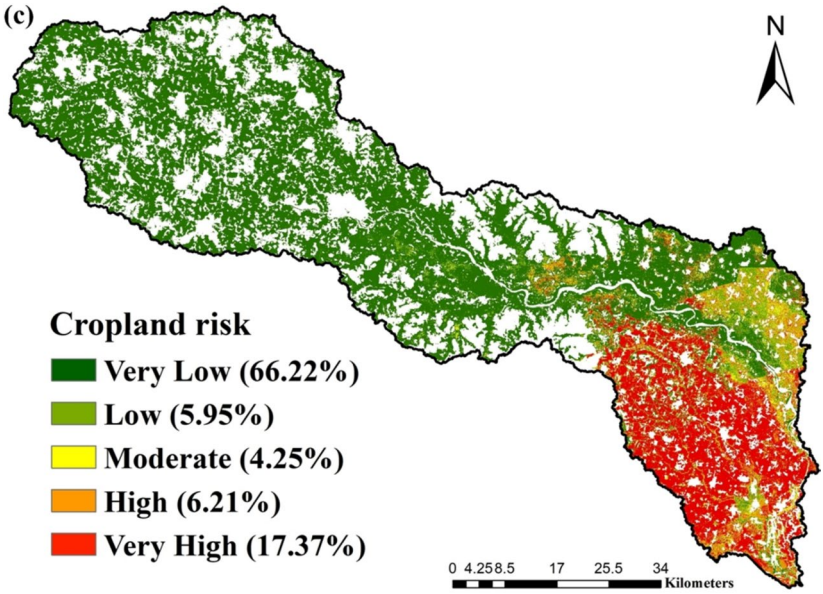

Fig. 13 (continued)

inundation impacts on cropland, affecting 35.93% of the total farmland through S1 C band images. This data on associated damage could be advantageous for disaster management and emergency response efforts in the area studied.

In the Dwarakeswar basin, peak river discharge typically occurs 1 to 2 days after heavy rainfall in the upper catchment during the monsoon (Fig. 13b). From 1972 to 2020, the annual peak discharges ranged from 11.33 to 3132.44 m^3/s, influencing flood events in the area. Flows above 800 m^3/s exceed the danger level, with 1000 m^3/s marking significant flood events. Peak discharges increased until 1995, then declined. The highest recorded discharge was 3111.44 m^3/s on September 27, 1995, exceeding the extreme danger level of 77.11 m. The most significant flood occurred on September 1, 1978, at Bankura, with a discharge of 3132 m^3/s.

The XAI SHAP method utilized in this study facilitated the influence of input factors for FSM analysis. It was found that rainfall, MNDWI, elevation, NDVI, distance from the river, drainage density, and TRI were identified as the most influential conditioning factors for FSM modeling. These findings are consistent with several recent studies (Aydin and Iban 2022; Wang et al. 2023). This study presented future FSM using the CMIP6 model under SSP2 4.5 and SSP5 8.5 scenarios (1990–2030). Previous studies by Hirabayashi et al. (2021) examined future flood risk projections based on CMIP6 climate models. However, consistent projections from models within the same institute offer hope for reducing uncertainties. The AHP-GBM model with SSP2 4.5 and SSP5 8.5 scenarios showed that the susceptibility to flooding across the study area varies, with the majority of the area falling into the very low susceptibility class. Specifically, under the SSP2 4.5 scenario, the distribution of susceptibility classes ranged from very low (64.63%) to very high (15.67%). In the SSP245 scenario, the respective percentages were from 59.73% for very low to 17.69% for very high susceptibility. Under the SSP5 8.5 scenario, areas categorized from very low to very high susceptibility were 56.10% and 18.10%, respectively. All models identified the

southern part of the study area as particularly vulnerable to future flooding due to climate change.

The outcomes of this study could offer valuable insights for flood hazard managers or researchers in determining the most appropriate techniques for FSM. One limitation of this study is its exploring methodologies for conducting flood research in scenarios where data is entirely absent, which warrants further investigation. Although the classifiers demonstrated effectiveness in a vast study area, there is an uneven distribution of flood samples across it. Such a heterogeneous distribution of samples could introduce bias in susceptibility prediction. Nonetheless, a significant drawback of the current approach is the absence of temporal variations and real-time flood data. Another primary limitation pertains to the methods employed and FSM in general, as these maps solely indicate areas prone to flooding without providing details on flood depth or velocity. It is suggested that future investigations, such as this one, integrate hydraulic modeling, capable of generating 2D maps depicting depth and velocity. Lastly, this paper does not address inter-annual or intra-annual variations of climatic parameters. Utilizing monthly or daily input data could provide a deeper understanding of the impact of meteorological conditions. Additionally, the increased resolution of input datasets and the availability of conditioning factor datasets could also impact the results of susceptibility maps. This study can be extended to assess the prediction accuracy of the model in diverse terrain environments.

5.1 Some suggestion

Different nature-based solution approaches, such as wetland restoration, creating water retention zones, clearing barriers, revitalizing former waterways, and integrating with traditional infrastructure, have enhanced flood protection efforts. These green strategies have proven to be effective in mitigating flood risks in recent times.

Several nature-based solutions can be employed as part of flood risk mitigation strategies:

- Wetland restoration: Reinstating natural wetland habitats can help absorb excess water during floods, reducing their impact on surrounding areas.
- Riparian buffer zones: planting vegetation along riverbanks can stabilize soil, prevent erosion, and absorb floodwaters, acting as a natural barrier.
- Floodplain reconnection: allowing rivers to naturally overflow into their floodplains can reduce the force of floods downstream by spreading water across a wider area.
- Green infrastructure: Implementing green roofs, permeable pavements, and rain gardens can absorb rainfall and reduce surface runoff, thus lowering the risk of urban flooding.
- Ecosystem-based approaches: Utilizing natural ecosystems such as forests, grassland, and dunes can act as buffers against storm surges and tidal flooding, protecting coastal communities.
- Constructed wetlands: Building artificial wetlands can mimic the functions of natural wetlands, providing storage for excess water and improving water quality.
- Regenerative agriculture: Practices such as mixed farming, cover cropping, climate-resilient agriculture, and agroforestry can enhance climate change adaptation, soil health and water retention, reducing runoff and flooding.
- Natural channel design: Restoring streams and rivers to their natural, meandering state can improve their capacity to convey floodwaters and reduce erosion.

- Community engagement and education: involving local communities in flood risk management and raising awareness about nature-based solutions can enhance their acceptance and effectiveness

6 Conclusion

This study utilized hybrid AHP-based ML methods (i.e., AHP-RF, AHP-XGB, AHP-GBM, AHP-glmboost, AHP-glmnet, and AHP-rda) for FSM in the Dwarakeswar river basin, eastern India. The models were developed using a spatial database comprising fifteen flood conditioning factors related to topography, climate, hydrology, terrain distribution, and historical flood data derived from past flooding events observed via Sentinel-1 imagery and Global flood database in the GEE cloud. The significance of these factors was assessed through various diagnostic tests for Pearson correlation, OLS, and multicollinearity, including VIF score, as well as an InGR test. The outcomes of these tests indicated the absence of multicollinearity issues among the chosen flood conditioning factors. The multicollinearity test demonstrated that all factors had VIF scores below 10, indicating the absence of multicollinearity issues among the flood conditioning factors. The InGR test, however, indicated that rainfall (0.390), geology (0.367), MNDWI (0.344), elevation (0.263), and NDVI (0.259) emerge as the most significant factors, showing high InGR values compared to other influencing factors.

The accuracy of the studied models during the validation phases was assessed using various statistical metrics such as accuracy, kappa score, sensitivity, specificity, NPV, PPV, and AUC. The validation outcomes indicated satisfactory performance across all models examined, with the AHP-GBM model exhibiting the highest performance through the AUC of 0.996. Consequently, the AHP-GBM model emerges as a promising option for developing flood susceptibility maps. Findings revealed that AHP-GBM predicted 12.68% area as a very high susceptibility class, followed by 5.14% area (high), 3.81% area (moderate), 5.55% area (low), and 72.82% area (very low), respectively. The SHAP findings underscore the impact of different factors like rainfall, MNDWI, elevation, NDVI, proximity to rivers, drainage density, and TRI on flood susceptibility assessment. Based on the climate projections from future CMIP6 models (SSP2 4.5, SSP5 8.5), the southern region of the study area has been pinpointed as a hotspot for flooding vulnerability, with a susceptibility level classified as very high, encompassing 16.68% of the area.

The results of this study hold important policy relevance for flood management and disaster readiness within any river basin. By utilizing advanced ML methods combined with geospatial analysis, the research has effectively generated accurate FSM. These maps, along with the key contributing factors and the proven performance of different ML models, provide critical information to support informed decision-making and strengthen flood management efforts at both local and regional scales. Additionally, the FSM generated can inform land use planning in flood-prone areas, while the study's results overall contribute to the improvement of flood risk management across all vulnerable regions.

Supplementary Information The online version contains supplementary material available at https://doi.org/10.1007/s11069-025-07335-8.

Acknowledgements We also acknowledge Bhuvan, NRSC, ISRO, and the Central Water Commission (CWC), India, for their invaluable resources and support. Our gratitude extends to the European Space Agency (ESA) for providing open-access Sentinel-1 SAR images, and to Google Earth Engine for enabling geospatial data analysis and processing.

Funding No external funding.

Data availability The data that support the findings of this study are available from the corresponding author upon reasonable request.

Declarations

Competing interests This manuscript has not been published or presented elsewhere in part or entirety and is not under consideration by another journal. There are no conflicts of interest to declare.

Ethical approval Not applicable.

Consent to participate Not applicable.

Consent to publication Not applicable.

References

Ahmadlou M, Ebrahimian Ghajari Y, Karimi M (2022) Enhanced classification and regression tree (CART) by genetic algorithm (GA) and grid search (GS) for flood susceptibility mapping and assessment. Geocarto Int 37(26):13638–13657. https://doi.org/10.1080/10106049.2022.2082550

Ali SA, Parvin F, Pham QB et al (2020) GIS-based comparative assessment of flood susceptibility mapping using hybrid multi-criteria decision-making approach, naïve Bayes tree, bivariate statistics and logistic regression: a case of Topľa basin, Slovakia. Ecol Indic. https://doi.org/10.1016/j.ecolind.2020.106620

Al-Kindi KM, Alabri Z (2024) Investigating the role of the key conditioning factors in flood susceptibility mapping through machine learning approaches. Earth Syst Environ 8:63–81. https://doi.org/10.1007/s41748-023-00369-7

Arabameri A, Seyed Danesh A, Santosh M, Cerda A, Chandra Pal S, Ghorbanzadeh O, Chowdhuri I (2022) Flood susceptibility mapping using meta-heuristic algorithms. Geomat Nat Hazards Risk 13(1):949–974

Aydin HE, Iban MC (2022) Predicting and analyzing flood susceptibility using boosting-based ensemble machine learning algorithms with SHapley additive exPlanations. Nat Hazards 116(3):2957–2991. https://doi.org/10.1007/s11069-022-05793-y

Bui DT, Hoang ND, Martínez-Álvarez F, Ngo PTT, Hoa PV, Pham TD, Costache R (2020) A novel deep learning neural network approach for predicting flash flood susceptibility: a case study at a high frequency tropical storm area. Sci Total Environ 701:134413

Costache R, Popa MC, Tien Bui D et al (2020) Spatial predicting of flood potential areas using novel hybridizations of fuzzy decision-making, bivariate statistics, and machine learning. J Hydrol (Amst). https://doi.org/10.1016/j.jhydrol.2020.124808

Cui Y, Cai M, Stanley HE (2017) Comparative analysis and classifcation of cassette exons and constitutive exons. Biomed Res Int. https://doi.org/10.1155/2017/7323508

Das S (2018) Geographic information system and AHP-based flood hazard zonation of Vaitarna basin, Maharashtra, India. Arab J Geosci 11:576. https://doi.org/10.1007/s12517-018-3933-4

Das S, Pardeshi SD (2018) Morphometric analysis of Vaitarna and Ulhas river basins, Maharashtra, India: using geospatial techniques. Appl Water Sci 8:158. https://doi.org/10.1007/s13201-018-0801-z

Donnelly C, Kraus N, Larson M (2006) State of knowledge on measurement and modeling of coastal overwash. J Coast Res 22:965–991. https://doi.org/10.2112/04-0431.1
Douglas EM, Vogel RM, Kroll CN (2000) Trends in floods and low flows in the United States: impact of spatial correlation. J Hydrol 240(1–2):90–105
Duong Thi L, Van Do T, Le Van H (2020) Detection of flash-flood potential areas using watershed characteristics: application to Cau River watershed in Vietnam. J Earth Syst Sci 129:120. https://doi.org/10.1007/s12040-020-01386-0
Edamo ML, Ukumo TY, Lohani TK, Ayana MT, Ayele AM, Mada ZM, Abdi DM (2022) A comparative assessment of multi-criteria decision-making analysis and machine learning methods for flood susceptibility mapping and socio-economic impacts on flood risk in Abela-Abaya floodplain of Ethiopia. Environ Chall 9:100629. https://doi.org/10.1016/j.envc.2022.100629
Fatah KK, Mustafa YT (2022) Flood susceptibility mapping using an analytic hierarchy process model based on remote sensing and GIS approaches in Akre District, Kurdistan Region Iraq. Iraqi Geol J 55:123–151
Friedman J (1989) Regularized discriminant analysis. J Am Stat Assoc 84:165–175
Friedman J, Hastie T, Tibshirani R (2010) Regularization paths for generalized linear models via coordinate descent. J Stat Softw 33(1):1–22
Gai L et al (2019) Assessing the impact of human interventions on floods and low flows in the Wei River Basin in China using the LISFLOOD model. Sci Total Environ 653:1077–1094. https://doi.org/10.1016/j.scitotenv.2018.10.379
Ghobadi M, Ahmadipari M (2024) Enhancing flood susceptibility modeling: a hybrid deep neural network with statistical learning algorithms for predicting flood prone areas. Water Resour Manag. https://doi.org/10.1007/s11269-024-03770-7
Ghosh B (2023) Flood susceptibility assessment and mapping in a monsoon-dominated tropical river basin using GIS-based data-driven bivariate and multivariate statistical models and their ensemble techniques. Environ Earth Sci 82:28. https://doi.org/10.1007/s12665-022-10696-z
Ghosh B (2024) Assessing the effects of human interventions on the morphodynamics and health of a lowland tropical river: a case study of the river Dwarkeswar, India. Geosyst Geoenviron 3(1):100234
Haghizadeh A, Siahkamari S, Haghiabi AH, Rahmati O (2017) Forecasting flood-prone areas using Shannon's entropy model. J Earth Syst Sci 126:1–11. https://doi.org/10.1007/s12040-017-0819-x
Hammami S, Zouhri L, Souissi D et al (2019) Application of the GIS based multi-criteria decision analysis and analytical hierarchy process (AHP) in the flood susceptibility mapping (Tunisia). Arab J Geosci. https://doi.org/10.1007/s12517-019-4754-9
Han-Qiu X (2005) A study on information extraction of water body with the modified normalized difference water index (MNDWI). Natl Remote Sens Bull. https://doi.org/10.11834/jrs.20050586
Hirabayashi Y, Tanoue M, Sasaki O et al (2021) Global exposure to flooding from the new CMIP6 climate model projections. Sci Rep 11:3740. https://doi.org/10.1038/s41598-021-83279-w
Hitouri S, Mohajane M, Lahsaini M, Ali SA, Setargie TA, Tripathi G, D'Antonio P, Singh SK, Varasano A (2024) Flood susceptibility mapping using SAR data and machine learning algorithms in a small watershed in Northwestern Morocco. Remote Sens 16:858. https://doi.org/10.3390/rs16050858
Hosseini FS et al (2020) Flash-flood hazard assessment using ensembles and Bayesian-based machine learning models: application of the simulated annealing feature selection method. Sci Total Environ 711:135161. https://doi.org/10.1016/j.scitotenv.2019.135161
Islam ABT, Talukdar S, Mahato S, Kundu S, Eibek KU, Pham QB, Linh NTT (2021) Flood susceptibility modelling using advanced ensemble machine learning models. Geosci Front 12(3):101075. https://doi.org/10.1016/j.gsf.2020.09.006
Islam ABT, Bappi MMR, Alqadhi S, Bindajam AA, Mallick J, Talukdar S (2023) Improvement of flood susceptibility mapping by introducing hybrid ensemble learning algorithms and high-resolution satellite imageries. Nat Hazards 119:1–37. https://doi.org/10.1007/s11069-023-06106-7
Jenkins K, Hall J, Glenis V, Kilsby C (2018) A probabilistic analysis of surface water flood risk in London. Risk Anal 38:1169–1182. https://doi.org/10.1111/risa.12930
Jenks GF (1967) The data model concept in statistical mapping. Int Yearb Cartogr 7:186–190
Kannapiran UM, Bhaskar AS (2024) Flood inundation mapping of upstream region in the Adyar River basin: integrating hydrologic engineering centre's river analysis system (HEC-RAS) approach with groundwater considerations. Groundw Sustain Dev 24:101085. https://doi.org/10.1016/j.gsd.2024.101085
Kaya CM, Derin L (2023) Parameters and methods used in flood susceptibility mapping: a review. J Water Clim Change 14(6):1935–1960

Khodaei H, Nasiri Saleh F, Nobakht Dalir A, Zarei E (2025) Future flood susceptibility mapping under climate and land use change. Sci Rep 15:12394. https://doi.org/10.1038/s41598-025-97008-0
Khosravi K, Shahabi H, Pham BT, Adamowski J, Shirzadi A, Pradhan B, Prakash I (2019) A comparative assessment of flood susceptibility modeling using multi-criteria decision-making analysis and machine learning methods. J Hydrol 573:311–323. https://doi.org/10.1016/j.jhydrol.2019.03.073
Kourgialas NN, Karatzas GP (2011) Flood management and a GIS modelling method to assess flood-hazard areas—a case study. Hydrol Sci J 56:212–225. https://doi.org/10.1080/02626667.2011.555836
Liu J, Wang J, Xiong J, Cheng W, Li Y, Cao Y, Yang G (2022) Assessment of flood susceptibility mapping using support vector machine, logistic regression and their ensemble techniques in the Belt and Road region. Geocarto Int 37(25):9817–9846. https://doi.org/10.1080/10106049.2022.2025918
Lundberg S, Lee SI (2017) A unified approach to interpreting model predictions. In: Advances in neural information processing systems. https://doi.org/10.48550/arXiv.1705.07874
Mahmoud SH, Gan TY (2018) Multi-criteria approach to develop flood susceptibility maps in arid regions of Middle East. J Clean Prod 196:216–229. https://doi.org/10.1016/j.jclepro.2018.06.047
Malik S, Pal SC, Chowdhuri I, Chakrabortty R, Roy P, Das B (2020) Prediction of highly flood prone areas by GIS based heuristic and statistical model in a monsoon dominated region of Bengal Basin. Remote Sens Appl Soc Environ 19:100343. https://doi.org/10.1016/j.rsase.2020.100343
Mayr A, Binder H, Gefeller O, Schmid M (2014) The evolution of boosting algorithms from machine learning to statistical modelling. Methods Inf Med 53(6):419–427. https://doi.org/10.3414/me14-01-0077
Mfondoum AHN, Nguet PW, Seuwui DT et al (2023) Stepwise integration of analytical hierarchy process with machine learning algorithms for landslide, gully erosion and flash flood susceptibility mapping over the North-Moungo perimeter, Cameroon. Geoenviron Disasters 10:22. https://doi.org/10.1186/s40677-023-00254-5
Mitra R, Saha P, Das J (2022) Assessment of the performance of GIS-based analytical hierarchical process (AHP) approach for flood modelling in Uttar Dinajpur district of West Bengal, India. Geomat Nat Hazards Risk 13(1):2183–2226
Mojaddadi H, Pradhan B, Nampak H, Ahmad N, Ghazali AHB (2017) Ensemble machine-learning-based geospatial approach for flood risk assessment using multi-sensor remote-sensing data and GIS. Geomat Nat Hazards Risk 8(2):1080–1102. https://doi.org/10.1080/19475705.2017.1294113
Mosavi A, Golshan M, Janizadeh S, Choubin B, Melesse AM, Dineva AA (2022) Ensemble models of GLM, FDA, MARS, and RF for flood and erosion susceptibility mapping: a priority assessment of sub-basins. Geocarto Int 37(9):2541–2560. https://doi.org/10.1080/10106049.2020.1829101
Muthusamy M, Casado MR, Butler D, Leinster P (2021) Understanding the effects of digital elevation model resolution in urban fluvial flood modelling. J Hydrol 596:126088. https://doi.org/10.1016/j.jhydrol.2021.126088
Nachappa TG, Piralilou ST, Gholamnia K, Ghorbanzadeh O, Rahmati O, Blaschke T (2020) Flood susceptibility mapping with machine learning, multi-criteria decision analysis and ensemble using Dempster Shafer theory. J Hydrol 590:125275. https://doi.org/10.1016/j.jhydrol.2020.12527
National Disaster Management Authority (NDMA) (2021) Annual flood report, flood hazard atlas–West Bengal–a geospatial approach version-1 (2000–2020), irrigation and water ways directorate government of west Bengal. URL: www.ndma.gov.in. Accessed 24 Mar 2024
Ngo PT, Hoang N, Pradhan B, Nguyen QK, Tran XT, Nguyen QM, Nguyen VN, Samui P, Bui DT (2018) A novel hybrid swarm optimized multilayer neural network for spatial prediction of flash floods in tropical areas using Sentinel-1 SAR imagery and geospatial data. Sensors 18(11):3704. https://doi.org/10.3390/s18113704
Nguyen DH (2022) Flood susceptibility assessment using hybrid machine learning and remote sensing in Quang Tri province, Vietnam. Trans GIS 26(7):2776–2801. https://doi.org/10.1111/tgis.12980
Nguyen TT, Hoang AH (2023) Flash flood hazard mapping using landsat-8 imagery, Ahp, and Gis in the Ngan Sau and Ngan Pho River basins, North-Central Vietnam. Geogr Environ Sustain 16(2):57–67
Nsangou D, Kpoumié A, Mfonka Z, Ngouh AN, Fossi DH, Jourdan C, Mbele HZ, Mouncherou OF, Vandervaere JP, Ndam Ngoupayou JR (2022) Urban flood susceptibility modelling using AHP and GIS approach: case of the Mfoundi watershed at Yaoundé in the South-Cameroon plateau. Sci Afr 15:e01043. https://doi.org/10.1016/j.sciaf.2021.e01043
Otsu N (1979) Threshold selection method from gray-level histograms. IEEE Trans Syst Man Cybern. https://doi.org/10.1109/tsmc.1979.4310076
Penki R, Basina SS, Tanniru SR (2023) Application of geographical information system-based analytical hierarchy process modeling for flood susceptibility mapping of Krishna District in Andhra Pradesh. Environ Sci Pollut Res 30(44):99062–99075
Plataridis K, Mallios Z (2023) Flood susceptibility mapping using hybrid models optimized with artificial Bee Colony. J Hydrol 624:129961. https://doi.org/10.1016/j.jhydrol.2023.129961

Pourali SH, Arrowsmith C, Chrisman N, Matkan AA, Mitchell D (2014) Topography wetness index application in flood-risk-based land use planning. Appl Spat Anal Policy 9(1):39–54. https://doi.org/10.1007/s12061-014-9130-2

Quinlan JR (1986) Induction of decision trees. Mach Learn 1(1):81–106. https://doi.org/10.1007/BF00116251

Rahmati O, Zeinivand H, Besharat M (2016) Flood susceptibility mapping using frequency ratio and logistic regression models. Arab J Geosci 9:1–17. https://doi.org/10.1007/s12517-015-2225-8

Rahmati O, Kalantari Z, Samadi M et al (2019) GIS-based site selection for check dams in watersheds: considering geomorphometric and topo hydrological factors. Sustainability (Switzerland). https://doi.org/10.3390/su11205639

Rouse JW, Haas RH, Schell JA, Deering DW (1974) Monitoring vegetation systems in the great plains with ERTS. NASA Spec Publ 351:309–317

Roy SK (2019) Flood as a catastrophic hazards on Dwarakeswar river basin. Int J Sci Dev Res 4(8):6–13

Saaty TL (1980) The analytical hierarchy process. McGraw-Hill, New York

Saaty RW (1987) The analytic hierarchy process—what it is and how it is used. Math Model 9(3–5):161–176. https://doi.org/10.1016/0270-0255(87)90473-8

Sahana M, Pham BT, Shukla M, Costache R, Thu DX, Chakrabortty R, Satyam N, Nguyen HD, Van Phong T, Van Le H, Pal SC, Areendran G, Imdad K, Prakash I (2020) Rainfall induced landslide susceptibility mapping using novel hybrid soft computing methods based on multi-layer perceptron neural network classifier. Geocarto Int 37(10):2747–2771. https://doi.org/10.1080/10106049.2020.1837262

Sahoo S, Sil I, Dhar A, Debsarkar A, Das P, Kar A (2018) Future scenarios of land-use suitability modeling for agricultural sustainability in a river basin. J Clean Prod 205:313–328. https://doi.org/10.1016/j.jclepro.2018.09.099

Sahoo S, Singha C, Govind A (2024) Prediction of pulse suitability in rice fallow areas using fuzzy AHP-based machine learning methods in Eastern India. Paddy Water Environ 22(3):341–359. https://doi.org/10.1007/s10333-024-00970-0

Samal NR, Roy PK, Majumadar M, Bhattacharya S, Biswasroy M (2014) Six years major historical urban floods in West Bengal state in India: comparative analysis using neuro-genetic model. Am J Water Resour 2(2):41–53

Samanta RK, Bhunia GS, Shit PK, Pourghasemi HR (2018a) Flood susceptibility mapping using geospatial frequency ratio technique: a case study of Subarnarekha River Basin, India. Model Earth Syst Environ 4:395–408

Samanta S, Pal DK, Palsamanta B (2018b) Flood susceptibility analysis through remote sensing, GIS and frequency ratio model. Appl Water Sci. https://doi.org/10.1007/s13201-018-0710-1

Sameen MI, Sarkar R, Pradhan B, Drukpa D, Alamri AM, Park H (2019) Landslide spatial modelling using unsupervised factor optimisation and regularised greedy forests. Comput Geosci 134:104336. https://doi.org/10.1016/j.cageo.2019.104336

Seydi ST, Kanani-Sadat Y, Hasanlou M, Sahraei R, Chanussot J, Amani M (2023) Comparison of machine learning algorithms for flood susceptibility mapping. Remote Sens 15:192. https://doi.org/10.3390/rs15010192

Shahabi H, Shirzadi A, Ronoud S, Asadi S, Pham BT, Mansouripour F, Geertsema M, Clague JJ, Bui DT (2020) Flash flood susceptibility mapping using a novel deep learning model based on deep belief network, back propagation and genetic algorithm. Geosci Front 12(3):101100. https://doi.org/10.1016/j.gsf.2020.10.007

Shrestha N (2020) Detecting multicollinearity in regression analysis. AJAMS 8:39–42. https://doi.org/10.12691/ajams-8-2-1

Shu EG, Porter JR, Hauer ME et al (2023) Integrating climate change induced flood risk into future population projections. Nat Commun 14:7870. https://doi.org/10.1038/s41467-023-43493-8

Siddayao GP, Valdez SE, Fernandez PL (2014) Analytic hierarchy process (AHP) in spatial modeling for floodplain risk assessment. Int J Mach Learn Comput 4(5):450

Singha C, Swain KC (2022) Spatial Analyses of cyclone amphan induced flood inundation mapping using Sentinel-1A SAR images through GEE cloud. In: Bansal JC, Engelbrecht A, Shukla PK (eds) Computer vision and robotics. Algorithms for intelligent systems. Springer, Singapore

Singha C, Swain KC, Meliho M, Abdo HG, Almohamad H, Al-Mutiry M (2022) Spatial analysis of flood hazard zoning map using novel hybrid machine learning technique in Assam, India. Remote Sens 14:6229. https://doi.org/10.3390/rs14246229

Singha C, Gulzar S, Swain KC, Pradhan D (2023) Apple yield prediction mapping using machine learning techniques through the Google Earth Engine cloud in Kashmir Valley, India. J Appl Remote Sens 17(1):014505. https://doi.org/10.1117/1.JRS.17.014505

Singha C, Rana VK, Pham QB, Nguyen DC, Łupikasza E (2024) Integrating machine learning and geospatial data analysis for comprehensive flood hazard assessment. Environ Sci Pollut Res 31(35):48497–48522. https://doi.org/10.1007/s11356-024-34286-7

Singha C, Sahoo S, Mahtaj AB, Moghimi A, Welzel M, Govind A (2025) Advancing flood risk assessment: multitemporal SAR-based flood inventory generation using transfer learning and hybrid fuzzy-AHP-machine learning for flood susceptibility mapping in the Mahananda River Basin. J Environ Manag 380:124972. https://doi.org/10.1016/j.jenvman.2025.124972

Skilodimou HD, Bathrellos GD, Alexakis DE (2021) Flood hazard assessment mapping in burned and urban areas. Sustainability 13(8):4455. https://doi.org/10.3390/su13084455

Soltani K, Ebtehaj I, Amiri A, Azari A, Gharabaghi B, Bonakdari H (2021) Mapping the spatial and temporal variability of flood susceptibility using remotely sensed normalized difference vegetation index and the forecasted changes in the future. Sci Total Environ 770:145288. https://doi.org/10.1016/j.scitotenv.2021.145288

Souissi D, Zouhri L, Hammami S et al (2020) GIS-based MCDM–AHP modeling for flood susceptibility mapping of arid areas, southeastern Tunisia. Geocarto Int 35:991–1017. https://doi.org/10.1080/10106049.2019.1566405

Stefanidis S, Stathis D (2013) Assessment of flood hazard based on natural and anthropogenic factors using analytic hierarchy process (AHP). Nat Hazards J Int Soc Prev Mitig Nat Hazards 68(2):569–585

Strickland J (2016) Data analytics using open-source tools. Lulu.Com, Morrisville

Sun X, Li R, Shan X, Xu H, Wang J (2021) Assessment of climate change impacts and urban flood management schemes in central Shanghai. Int J Disaster Risk Reduct 65:102563. https://doi.org/10.1016/j.ijdrr.2021.102563

Swain KC, Singha C, Nayak L (2020) Flood susceptibility mapping through the GIS-AHP technique using the cloud. ISPRS Int J Geo-Inf 9:720. https://doi.org/10.3390/ijgi9120720

Tabari H (2020) Climate change impact on flood and extreme precipitation increases with water availability. Sci Rep 10:13768. https://doi.org/10.1038/s41598-020-70816-2

Talukdar S et al (2022) Application of hybrid machine learning algorithms for flood susceptibility modeling. In: Pradhan B, Shit PK, Bhunia GS, Adhikary PP, Pourghasemi HR (eds) Spatial modelling of flood risk and flood hazards. GIScience and geo-environmental modelling. Springer, Cham. https://doi.org/10.1007/978-3-030-94544-2_7

Tehrany MS, Pradhan B, Jebur MN (2013) Spatial prediction of flood susceptible areas using rule based decision tree (DT) and a novel ensemble bivariate and multivariate statistical models in GIS. J Hydrol 504:69–79. https://doi.org/10.1016/j.jhydrol.2013.09.034

Tehrany MS, Pradhan B, Jebur MN (2014) Flood susceptibility mapping using a novel ensemble weights-of-evidence and support vector machine models in GIS. J Hydrol 512:332–343. https://doi.org/10.1016/j.jhydrol.2014.03.008

Tehrany MS, Kumar L, Jebur MN, Shabani F (2018) Evaluating the application of the statistical index method in flood susceptibility mapping and its comparison with frequency ratio and logistic regression methods. Geomat Nat Hazards Risk 10:79–101

Termeh SVR, Kornejady A, Pourghasemi HR, Keesstra S (2018) Flood susceptibility mapping using novel ensembles of adaptive neuro fuzzy inference system and metaheuristic algorithms. Sci Total Environ 615:438–451

Tripathi P (2015) Flood disaster in India: an analysis of trend and preparedness. Interdiscip J Contemp Res 2(4):91–98

Vashist K, Singh KK (2023) HEC-RAS 2D modeling for flood inundation mapping: a case study of the Krishna River Basin. Water Pract Technol 18(4):831–844. https://doi.org/10.2166/wpt.2023.048

Vilasan RT, Kapse VS (2022) Evaluation of the prediction capability of AHP and F-AHP methods in flood susceptibility mapping of Ernakulam district (India). Nat Hazards 112(2):1767–1793. https://doi.org/10.1007/s11069-022-05248-4

Wang Y, Hong H, Chen W, Li S, Pamučar D, Gigović L, Drobnjak S, Tien Bui D, Duan H (2019) A hybrid GIS multi-criteria decision-making method for flood susceptibility mapping at Shangyou, China. Remote Sens 11:62. https://doi.org/10.3390/rs11010062

Wang M, Li Y, Yuan H, Zhou S, Wang Y, Ikram RMA, Li J (2023) An XGBoost-SHAP approach to quantifying morphological impact on urban flooding susceptibility. Ecol Ind 156:111137. https://doi.org/10.1016/j.ecolind.2023.111137

Waqas H, Lu L, Tariq A et al (2021) Flash flood susceptibility assessment and zonation using an integrating analytic hierarchy process and frequency ratio model for the Chitral district, Khyber Pakhtunkhwa, Pakistan. Water (Switzerland). https://doi.org/10.3390/w13121650

Wubalem A, Tesfaw G, Dawit Z, Getahun B, Mekuria T, Jothimani M (2021) Comparison of statistical and analytical hierarchy process methods on flood susceptibility mapping: In a case study of the Lake Tana sub-basin in northwestern Ethiopia. Open Geosci 13(1):1668–1688

Xu H (2006) Modification of normalised difference water index (NDWI) to enhance open water features in remotely sensed imagery. Int J Remote Sens 27(14):3025–3033. https://doi.org/10.1080/01431160600589179

Zdaniuk B (2014) Ordinary least-squares (OLS) model. In: Michalos AC (ed) Encyclopedia of quality of life and well-being research. Springer, Dordrecht. https://doi.org/10.1007/978-94-007-0753-5_2008

Zeng Z, Lai C, Wang Z, Chen Y, Chen X (2024) Future sea level rise exacerbates compound floods induced by rainstorm and storm tide during super typhoon events: a case study from Zhuhai, China. Sci Total Environ 911:168799. https://doi.org/10.1016/j.scitotenv.2023.168799

Zhu K, Lai C, Wang Z, Zeng Z, Mao Z, Chen X (2024) A novel framework for feature simplification and selection in flood susceptibility assessment based on machine learning. J Hydrol Reg Stud 52:101739. https://doi.org/10.1016/j.ejrh.2024.101739

Authors and Affiliations

Chiranjit Singha[1] · Neha Chakraborty[2] · Satiprasad Sahoo[3,4] · Quoc Bao Pham[5] · Yunqing Xuan[6]

✉ Quoc Bao Pham
quoc_bao.pham@us.edu.pl

[1] Department of Agricultural Engineering, Institute of Agriculture, Visva-Bharati (A Central University), Sriniketan, Birbhum 731236, India

[2] Maulana Abul Kalam Azad University of Technology, Kolkata 700064, India

[3] International Center for Agricultural Research in the Dry Areas (ICARDA), 2 Port Said, Victoria Sq, Ismail El-Shaaer Building, Maadi, Cairo 11728, Egypt

[4] Prajukti Research Private Limited, Baruipur, West Bengal 743610, India

[5] Faculty of Natural Sciences, Institute of Earth Sciences, University of Silesia in Katowice, Będzińska street 60, 41-200 Sosnowiec, Poland

[6] Faculty of Science and Engineering, Swansea University, Bay Campus, Fabian Way, Swansea SA1 8EN, UK